Production of High Mass Dielectrons in 800 GeV/c Proton-Nucleus Collisions

AUTHOR(S):

Toshida, Takuo

CITATION:

Toshida, Takuo. Production of High Mass Dielectrons in 800 GeV/c Proton-Nucleus Collisions. Memoirs of the Faculty of Science, Kyoto University. Series of physics, astrophysics, geophysics and chemistry 1988, 37(2): 93-138

ISSUE DATE:

1988-03

URL:

http://hdl.handle.net/2433/257599

Memoirs of the Faculty of Science, Kyoto University, Series of Physics, Astrophysics, Geophysics and Chemistry, Vol. XXXVII, No. 2, Article 2, 1988

Production of High Mass Dielectrons in 800 GeV/c Proton-Nucleus Collisions

By

Takuo YOSHIDA

Department of Physics, Faculty of Science, Kyoto University, Kyoto 606, Japan

(Received December 10, 1986)

Abstract

The production of dielectrons in proton-nucleus collisions has been measured. The incident proton momentum was 800 GeV/c. The Υ family of resonances and the continuous mass spectrum above 8 GeV/c^2 have been observed. The dielectron mass resolution was 0.15% to 0.20%. This high resolution is one of the remarkable features of the experiment. The Υ, Υ', and Υ'' were observed separately because of the high resolution. The mass spectrum of the continuum is compared with the naive Drell-Yan process. The production cross section times branching ratio of the Υ family of resonances has been measured. The production ratios between the Υ, Υ' and Υ'' are extracted. Comparing the yield of the Υ family of resonances with the continuum, our data indicates that the production ratio of the resonances to the continuum may be smaller than the results which were presented by other authors. The p_t distributions of the resonances and the continuum have been measured. The mean values of the p_t distributions are compared with the results of other experiments.

I. Introduction

Various experiments to measure the hadronic production of dileptons have been performed since Christenson et al. presented the first measurement of the dimuon mass spectrum in 1970 [1]. In fixed-target experiments, detecting dimuons is more favourable than detecting dielectrons, because muons are isolated easily by placing a block of heavy material just behind the target. This type of apparatus is called a closed aperture spectrometer. Hadrons and electrons are all absorbed in the material, and only muons penetrate the absorber. Moreover, the absorption of the background at the early stage reduces the counting rates of the particle detectors placed downstream, and makes it easy to increase the luminosity. On the other hand, this method has a defect that the mass resolution is restricted by the multiple scattering in the heavy material. The other type of apparatus is the so called open aperture spectrometer in which no absorber is placed in the aperture. However, this method has a defect that the target luminosity is restricted by the heavy background.

This paper presents a measurement of dielectron production with the open geometry spectrometer in 800 GeV/c proton-nucleus collisions:

$$p+N \rightarrow e^+ + e^- + X \tag{1}$$

The energy of the collisions corresponds to $\sqrt{s}=38.8$ GeV in the nucleon-nucleon center of mass system. The invariant mass region from 8 GeV/c² to 15 GeV/c² is studied. There are a few motivations in this study. One is to investigate the behavior of the continuous mass spectrum of high mass dielectrons, and another is to observe the Υ family of resonances which decay into e^+e^-. The apparatus was designed to achieve 0.15% to 0.2% resolution in the dielectron mass. This resolution is better than any other experiment which has been carried out so far to measure the hadronic dilepton production. The Υ, Υ' and Υ'' have been obseved separately beause of this high resolution. The third motivation of this measurement is to search for the differences between dielectron and dimuon yields, if any, because the open aperture spectrometer enabled us to observe both dielectrons and dimuons at the same time.

This experiment has been carried out at Fermi National Accelerator Laboratory (FNAL) as Experiment 605 by a collaboration of Columbia Univ., CERN, FNAL, KEK, Kyoto Univ., SACLAY, SUNY at Stony Brook, and Univ. of Washington.

I-1. The Drell-Yan Process

The continuous mass spectrum of the dileptons in hadronic collisions falls rapidly with increasing mass. This has been described theoretically by the Drell-Yan process [2], where a quark in one hadron and an anti-quark in an-other hadron annihilate into a virtual photon which decays into a lepton pair. This process is shown schematically in Figure 1. When the dilepton is massive compared to the nucleon, the time scale for this process must be much shorter than that of other interactions between the quarks in the hadrons. So, the annihilating quarks have no time to be affected by the other quarks in the hadrons during this process. In this case, the annihilating quarks can be regarded as asymptotically free particles, and the other quarks only spectators.

The differential cross section for the naive Drell-Yan process [3] is written as

$$m^3\frac{\mathrm{d}^2\sigma}{\mathrm{d}m\mathrm{d}y}=\frac{8\pi\alpha^2\tau}{9}\sum_i e_i^2\{q_i^{h_1}(x_1)\bar{q}_i^{h_2}(x_2)+\bar{q}_i^{h_1}(x_1)q_i^{h_2}(x_2)\}, \tag{2}$$

with

$$x_1=\sqrt{\tau}\,\mathrm{e}^{y},\quad x_2=\sqrt{\tau}\,\mathrm{e}^{-y}, \tag{3}$$

where m is the dilepton mass, y is the rapidity, $\sqrt{\tau}\equiv m/\sqrt{s}$ is the dilepton mass over the invariant mass of the nucleon-nucleon system, α is the fine structure constant, $q_i^h(x)$ or $\bar{q}_i^h(x)$ is the distribution function of the quark or anti-quark of flavour i, i.e. the density of the quark or anti-quark carrying the momentum fraction x of the parent

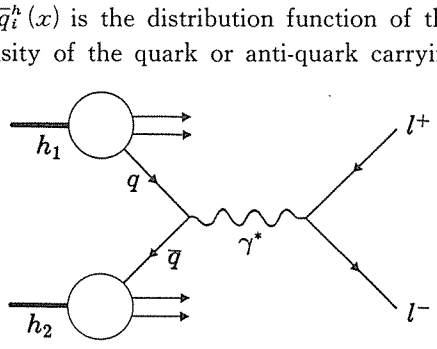

Figure 1. Diagram for the Drell-Yan process.

hadron h, and e_i, is the fractional charge of the quark. The sum must be performed over all the quark flavours; a factor 1/3 for colour conservation has been incorporated in the numerical factor 1/9 in the equation. The rapidity y is defined by

$$y \equiv \frac{1}{2}\ln\left(\frac{E+p_l}{E-p_l}\right) = \frac{1}{2}\ln\left(\frac{x_1}{x_2}\right), \tag{4}$$

where E and p_l are the energy and longitudinal momentum of the dilepton in the nucleon-nucleon center of mass system.

The naive Drell-Yan process implies the following properties.

1. The cross-section is calculable using the quark distribution functions determined by deep inelastic scattering experiments.
2. $m^3 d^2\sigma/dmdy$ scales with τ.
3. The p_t of the dilepton is derived from the intrinsic transverse momenta of the quarks in hadrons. Thus, the mean value of the p_t distribution is expected to be about 0.5 GeV/c [3].
4. The decay angular distribution of the lepton pairs follows $(1+\cos^2\theta^*)$ in the dilepton rest frame [3], where the θ^* is an angle between the outgoing lepton and the incoming quark.

The scaling rule and the decay angular distribution have been confirmed within the experimental errors [4, 5]. However, this naive model disagrees with measurements in detail. First, this model cannot explain the measured p_t distributions in which the mean value exceeds 1 GeV/c and increases with $\sqrt{s}$ [4, 6–10]. Second, although the shape of the experimental mass spectrum can be reproduced by this model, the calculated value of the cross section is smaller than the measurement by a factor of about 2 throughout the mass region which has been measured by various experiments so far [4, 9, 11, 12]. This factor is called the K factor.

Recently, the naive Drell-Yan process has been improved by taking into account QCD effects in which gluons mediate the strong interaction between quarks. When the momentum transfer is large, the quark-gluon coupling constant can be described as

$$\alpha_s(Q^2) = \frac{12\pi}{(33-2n_f)\ln(Q^2/\Lambda^2)}, \tag{5}$$

where Q is the momentum transfer, n_f is the number of quark flavours, and Λ is a scale constant of approximately 200 MeV/c. If Q is a silepton mass near the Υ region, α_s has a small value (approximately 0.2). This fact makes the perturbative approach reasonable. One of the important results of a perturbative QCD calculation is that the quark distribution function depends not only on the fractional momentum x but also on the Q^2. This is usually called "scale violation".

Moreover, it was suggested by theorists that the K factor came from the analytical continuation of the Q^2 dependence in the quark distribution functions from the spece-like deep inelastic scattering to the time-like Drell-Yan process [13]. If it is the case, the K factor is necessary as long as the quark distribution functions obtained in deep inelastic scattering are used.

The QCD effects also play an important role in the p_t distribution of dileptons.

Emitting or absorbing hard gluons at the annihilating quark lines gives an extra p_t-kick to the dilepton, and pushes up the mean value of the p_t distribution [3].

Thus, the Drell-Yan process has been a fruitful arena for QCD tests. So far, the measurements and theoretical interpretations of the Drell-Yan process have served to prove the validity of the standard model. Generally speaking, the Drell-Yan process is, as well as deep inelastic scattering, one of the best phenomena to test our knowledge on the internal structure of hadrons and our understanding of the fundamental interactions between the constituents of hadrons. The higher mass and higher p_t regions test the standard model most rigorously, because the larger momentum transfer probes the smallest structure in hadrons.

I-2. The Upsilon Resonances

In 1977, the Columbia-FNAL-Stony Brook collaboration (CFS) discovered three narrow resonances around 10 GeV/c^2 in the mass spectrum of dimuons produced in collisions of 400 GeV/c protons and Be target [14]. Later on, the three resonances were confirmed by e^+e^- collider experiments [15–17]. These resonances are referred to as Υ, Υ' and Υ'', and are interpreted as $b\bar{b}$ bound states by analogy with the J/ψ family which is interpreted as $c\bar{c}$ bound states. The phenomenological potential for $b\bar{b}$ system can explain the mass spacings of these resonances [18]. Since then, various new states and fine structures have been discovered in this mass region by e^+e^- collider experiments [19, 21]. The discovered states have been used to refine the potential model for heavy quarks [21].

While the Υ is produced via a virtual photon in e^+e^- collisions, the hadronic collisions produce such heavy quarks mostly through the strong interaction mediated by gluons. The lowest order processes in the strong interaction need two gluons in order to realize the colour singlet of the final state. In this case, the states with positive charge conjugation, i.e. χ_b states ($^3P_0$, $^3P_1$, $^3P_2$) are created first, and the subsequent radiative decay of the χ_b state produces the $\Upsilon(^3S_1)$. Carlson and Suaya [22] evaluated various diagrams for hadronic production of the Υ, and showed that the gluon amalgamation (fusion) model made the biggest contribution in nucleon-nucleon collisions. Therefore, the Υ production in hadronic collisions reflect the gluon distribution in hadrons. This is in remarkable contrast to the Drell-Yan process which reflects the quark distribution in hadrons. The difference in the production mechanism between the Υ and the Drell-Yan process manifests itself also in the distributions of various kinematical variables such as the transverse momentum, the rapidity, and the decay angle. So far, many authors have been observing the differences in the distributions of such variables [5, 6, 23]. The difference in the transverse momentum distributions is discussed in ChapterV.

The threshold for OZI (Okubo-Zweig-Iizuka) allowed decays of the $b\bar{b}$ states is about 10.55 GeV/c^2 [24]. Since the states above this threshold prefer to decay into B mesons through OZI allowed channels, only the states below the threshold can be seen in the dilepton spectrum. The fact that $\Upsilon''(3S)$ can be seen in the dilepton channel in hadronic collisions means that $\chi''_b(3P)$ state should be below the threshold for OZI allowed decays. The potential model also predicts the state around 10.50 GeV/c^2 [21].

However, χ''_b state has not directly found.

II. APPARATUS

II-1. Overview

The apparatus for this experiment was originally designed to perform simultaneous measurements of high p_t single production and high mass pair production of electrons, muons, and charged hadrons in hadronic collisions [25]. The apparatus is shown in Figure 2. An open aperture spectrometer was employed in order to accept electrons, hadrons, and muons simultaneously. The main problem of the open aperture geometry is in the background reduction. This problem is especially serious in the measurement of dilepton production. The small cross section for high mass dilepton production of a few picobarns/(GeV/c²) [4] forces us to increase the beam intensity as much as possible to gain luminosity. However, backgrounds which increase as the luminosity increases make the counting rates at the downstream detectors too high and degrade the measurements. In our experiment, powerful spectrometer magnets were placed immediately downstream of the target in order to sweep out the low momentum background particles from the aperture, and focus high mass pairs on the downstream detectors. A beam dump and a pair of collimators were placed in the magnet.

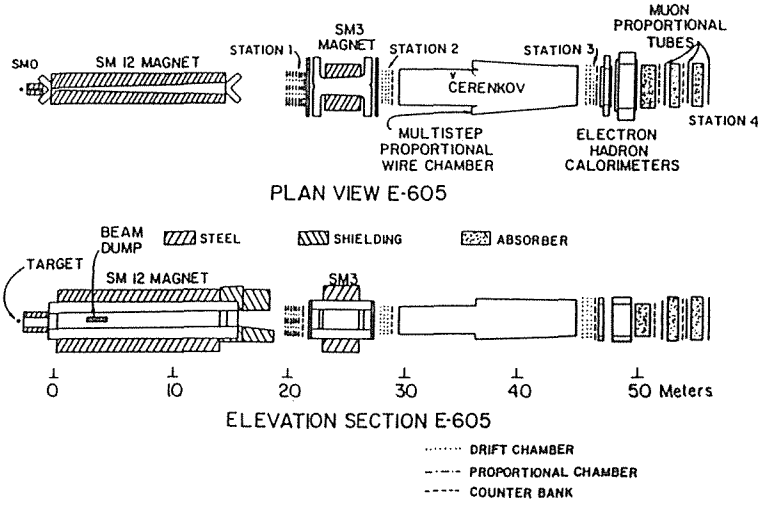

Figure 2. Schematic view of E605 apparatus.

The charged particles of interest were identified by the following detectors. The calorimeter distinguished electrons and hadrons by detecting the difference in shape between electromagnetic and hadronic showers developed in the dense material of the calorimeter. While electrons and hadrons were stopped in the calorimeter, muons easily penetrated the calorimeter and the additional absorbers behind the calorimeter. Therefore, muons were identified by the hodoscopes and the proportional tubes behind the calorimeter and the absorbers. The hadron species (π, K, p) were distinguished by the

ring imaging Cherenkov counter placed in frond of the calorimeter.

In the following descriptions on the details of the apparatus, a right-handed coordinate system is used, in which the z axis is defined along the beam direction, the y axis is defined to point vertically upwards, and consequently the x axis points in the horizontal direction consistent with a right-handed system. In addition, the u and v axes are defined in the $x-y$ plane. These additional axes point at an angle $\theta=\pm$ arctan (1/4) with respect to the y axis.

II-2. Beam and Targets

800 GeV/c protons extracted from FNAL Energy Saver to the Meson East beam line were used in this experiment. The protons were extracted once every 40 seconds. The spill duration was 12 seconds. Each spill was bunched into RF buckets. The RF bunches were 1 ns long each, and repeated every 18.9 ns in the spill. The position of the beam was monitored by single wire ionization chambers (SWICS) every 2 seconds during initial beam tuning. The SWICS were removed from the beam line during the data acquisition to avoid the backgrounds caused by them. The proton intensity was monitored by a secondary emission monitor (SEM) spill by spill during the data acquisition, and the information was recorded on the magnetic tape.

Three different sizes of thin horizontal metal strips were used as the targets. The sizes and other properties of the targets are listed in Table 1. Only the data with beryllium targets were used for the dielectron study. The tungsten target was not suitable for observing electrons, because electron bremsstrahlung in it seriously distorted the momenum of the electron. The targets were set horizontally in a target holder so as to minimize their vertical thickness, and consequently to minimize the secondary interactions of the outgoing particles.

Our vertical target thicknesses were comparable with the beam spot size. The targeting efficiency, i.e. the fraction of the beam hitting the target was monitored by the device called the 90 degree monitor which consisted of four scintillation counters. The 90 degree monitor viewed the target from a direction of 90 degrees with respect to the incident beam direction. The targeting efficiency was measured by recording the 90 degree monitor rates while moving the target up and down in units of one target thickness. Also, during the data acquisition, the information from the 90 degree monitor

Table 1 Properties of the targets

	Be(1)	Be(2)	W
Thickness(mm)	0.508	1.016	1.067
Length(mm)	55.9	58.7	13.1
Width(mm)	25	25	25
Density(g/cm^3)	1.848	1.848	19.3
A	9.01	9.01	183.9
Z	4	4	74
Absorption Length(cm)	36.7	36.7	10.3
Radiation Length(cm)	35.3	35.3	0.35

was recorded spill by spill on the magnetic tape. This was used to determine the targeting efficiency for each spill.

II-3. Magnets

Three dipole magnets, SM0, SM12, and SM3, were employed to measure the momenta of charged particles and to sweep out low momentum charged backgrounds. SM0 and SM12 were placed just behind the target and were followed by SM3. SM0 was a small magnet used to augment SM12 for some special runs. SM0 was turned off during this experiment.

SM12 was the largest one of these three magnets. The outside dimensions of its steel yoke were 14.4 m long, 2.7 m wide, and 5 m high. SM12 was operated at a current of 4000 amperes. The magnetic field was oriented horizontally, and the field intergral corresponded to a p_t-kick of 7.5 GeV/c in the vertical direction. The gap between the poles was tapered from 86.4 cm at the downstream exit to 15.7 cm at the upstream entrance. Because of the tapered gap, the horizontal component of the field, B_x, strongly depended on the z coordinate [26]. The gap was filled with helium gas to reduce the multiple scattering of the particles passing through the aperture.

SM3 was 3.23 m long, and its upstream aperture was 1.35 m wide and 1.68 m high. The gap between the poles was slightly tapered, and the downstream aperture was 1.5 m wide. SM3 was operated at a current of 4200 amperes. The magnetic field was oriented horizontally but in the opposite direction to the SM12 field. The field integral of SM3 corresponded to a p_t-kick of 0.914 GeV/c with the direction opposite to that of SM12. A helium gas bag was placed in the gap of SM3.

A horizontal elevation schematic of the interior of SM0 and SM12 is shown in Figure 3. A pair of tungsten collimators was placed at the entrance of SM12. In the middle of SM12, a beam dump was placed to absord the beam. The collimators and the beam dump absorbed low p_t particles emitted with vertical angles less than 37.1 milliradians. The beam dump consisted of a water-cooled copper block followed by lead and polyethylene absorbers. The copper block was 4.27 m long, and the front end of the block was tapered. The lead blocks were 0.76 m long in all. The polyethylene block was 0.94 m long, and absorbed neutrons.

Lead teeth were attached to the walls of SM12. These teeth absorbed photons emitted by π^0's. The shape of the teeth prevented the electromagnetic shower caused

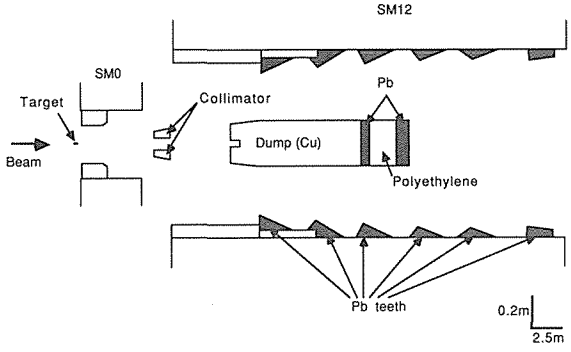

Figure 3. Interior of the SM12 magnet.

by the photons from illuminating the aperture of the downstream detectors.

II-4. Hodoscopes

As shown in Figure 2, there are 4 electronic tracking detector stations, Station 1,2,3, and 4, each of which has one or two planes of scintillation hodscopes and several planes of wire chambers. The configuration of these detectors and the name of each detector are shown in Figure 4 schematically.

The specifications of the hodoscopes are listed in Table 2. NA 110 plastic scintillator was employed as the material of the hodoscopes. The Y hodoscope planes were divided into left and right halves, and the X hodoscope planes were divided into up and down halves. Each half plane of the X and Y hodoscopes consisted of scintillator strips. The light from each scintillator strip was collected onto a Hamamatsu R329 phototube using a Plexiglas light guide. These hodoscopes produced fast trigger signals as described in Chapter III.

The X3 and Y3 hodoscopes located in front of the calorimeter had another role besides producing trigger signals. A 1.28 cm thick lead sheet was inserted between these two hodoscopes. Unlike a hadron or a muon, an electron begins to develop a shower in this lead sheet, and therefore gives a bigger pulse height in the Y3 hodoscope

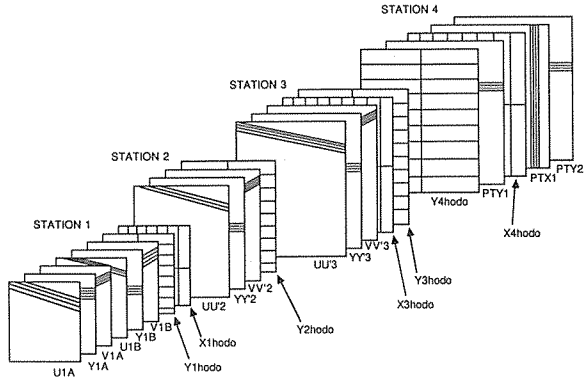

Figure 4. Configuration of chambers and hodoscopes.

Table 2 Specifications of the hodoscopes

	Position* z (cm)	Aperture x (cm)	Aperture y (cm)	Counter Length (cm)	Number of Counters
Y1	2046.9	121.9	152.4	61.0	2×12
X1	2050.7	121.9	152.4	76.2	2×12
Y2	2831.9	162.6	172.7	81.3	2×17
X3	4665,9	264.2	233.7	116.8	2×13
Y3	4691.9	264.2	233.7	132.1	2×13
Y4	5170.2	294.6	254.0	147.3	2×14
X4	5413.0	320.0	289.6	144.8	2×16

*Note that the target is at $z = -330$ cm

placed behind the lead sheet than a minimum ionizing particles. The pulse height of each counter in the X3 and Y3 hodoscopes was recorded on the deta tape, and was combined with the calorimeter data to identify electrons in the off-line analysis.

Station 4 was located behind the calorimeter. Since electrons and hadrons stopped in the calorimeter, the detectors at this station recorded only muons.

II-5. Wire Chambers

The specifications of the wire chambers are listed in Table 3. The signals from the wire chambers were essential for the track reconstruction in the off-line analysis.

Six multiwire proportional chambers (MWPC) were placed at Station 1. These chambers measured the y, u, and v coordinates of the charged particle trajectories. The wire spacing was 2 mm. Station 1 was the station closest to the target, and was exposed to higher radiation than other stations. Because of the high rate, the MWPC's were chosen, even though their spatial resolution was poorer than that of the drift chambers. The gas used for the MWPC's was a mixture of 25% (82.6%Ar/17%CO_2/0.4%Freon) and 75% (50%Ar/50%Ethane) bubbling through ethyl alcohol at $-6°C$.

Station 2 and Station 3 each had six drift chambers. These chambers also measured the y, u, and v coordinates. Neighboring planes, which have the same wire

Table 3 Specifications of the wire chambers

	Position* z (cm)	Aperture x (cm)	Aperture y (cm)	Wire Space (mm)	Number of Wires
	Station 1 MWPC's				
U1A	1896.8	128.3	151.4	1.97	896
Y1A	1922.0	128.3	149.6	2.07	736
V1A	1948.0	128.3	151.4	1.97	896
U1B	1973.5	128.3	151.4	1.97	896
Y1B	1998.6	128.3	149.6	2.03	736
V1B	2024.0	128.3	151.4	1.97	896
	Station 2 Drift Chambers				
UU'2	2752.3	167.6	182.9	9.86	208
YY'2	2777.2	167.6	178.8	10.16	176
VV'2	2802.4	167.6	182.9	9.86	208
	Station 3 Drift Cahmbers				
UU'3	4575.4	269.2	242.6	20.21	144
YY'3	4600.7	269.2	242.6	20.21	112
VV'3	4626.0	269.2	242.6	20.21	144
	Station 4 Proportional Tubes				
PTY1	5188.0	297.	305.	25.4	120
PTX1	5434.6	343.	309.	25.4	135
PTY2	5602.9	359.	364.	25.4	143

*Note that the target is at $z=-330$cm

direction, were staggered by one half of the cell width. The sense wire spacing was 1 cm in Station 2, and 2 cm in Station 3. The spatial resolution of these drift chambers was about 0.22 mm. The gas in the drift chambers was a mixture of 50% Ar and 50% ethane bubbling through ethyl alcohol at -6°C.

Three proportional tube planes were placed at Station 4 to measure the x and y positions of muons. Each plane consisted of two layers of proportional tube cells. The cell size was 2.5 cm$\times$2.5 cm. These two layers of each plane were staggered by half a cell to cover the dead region between each cell. These tubes were opetated with the same gas as the drift chambers.

II-6. Cherenkov Counter

A ring imaging Cherenkov counter [27] was designed to distinguish between hadron species (π, K, p) by measuring the emission angle of Cherenkov photons in helium gas. The information from this counter was not utilized to identify electrons or muons.

The 15.2 m long helium gas vessel was placed between Station 2 and Station 3. It was made of aluminum. The mirrors that reflect the Cherenkov photons to a multistep avalanche chamber were mounted near the downstream end in the gas vessel. The thickness of the mirrors was 2.22 cm. The gas vessel and the mirrors totalled 0.21 radiation lengths of material for electrons passing through the vessel. The effects caused by these materials were evaluated by a Monte Carlo simulation as described later.

II-7. Calorimeter

The calorimeter placed between Station 3 and Station 4 produced fast trigger signals for hadrons and electrons. Moreover, the information on the longitudinal shower development in the calorimeter served to distinguish hadrons and electrons in the off-line analysis. The details of the construction of the calorimeter are described elsewhere [26].

This calorimeter consisted of the electromagnetic part (EM part) and the hadronic part, as shown in Figure 5. The front surface of the EM part was 2.4 m high and 2.8 m wide. In the EM part, 32 layers of 6 mm thick plastic scintillators were arranged altermately with 3 mm thick lead sheets in the longitudinal direction. These layers were grouped into four modules E1, E2, E3, and E4 in the longitudinal direction with, 4, 9, 9, and 10 layers, respectively. Each module was divided into left and right halves, and each half was segmented vertically into twelve sections. An acrylic light guide and a phototube were attached to each segment in the EM part. The total thickness of the EM part was 19 radiation lengths. Therefore, electrons developed electromagnetic showers and stopped in the EM part. However, the material in the EM part corresponded to only 1 absorption length for hadrons. So, hadrons easily penetrated the EM part and reached the hadronic part placed behind the EM part.

The hadronic part had two modules in the longitudinal direction. The first module H1 consisted of 12 layers of 6 mm thick scintillators arranged alternately with 2.5 cm thick iron sheets, and the second module H2 consisted of 20 layers of 6 mm thick

scintillators arranged alternately with 5 cm thick iron sheets. The front surface of the hadronic part was 2.6 m high and 3 m wide. The total thickness was 8 absorption lengths including the EM part (1 absorption length). Each module in the hadronic part was divided into left and right halves, and each half was segmented vertically into thirteen sections. The light from each segment in the hadronic part was led to a phototube using a wave length shifter bar. The attenuation of the light along the wave shifter bar was corrected by masking the surface of the bar. The masked area increased toward the phototube.

Behind the calorimeter, a 102 cm thick zinc block and two 122 cm thick concrete blocks were placed to absorb any hadron shower leakage from the calorimeter. The detectors at Station 4 were placed between these blocks.

The dynode outputs of the phototubes in the calorimeter were sent to the calorimeter logic to produce trigger signals, and the anode outputs were read out by a quadratic ADC developed by D. Kaplan at Nevis Laboratory. In this ADC, the input charge and its digital output have a quadratic relation represented by

$$Q = a_0 + a_1 D + a_2 D^2 , \tag{6}$$

where Q is the input charge, and D is its digital output encoded in 8 bits. The parameters, a_0, a_1, and a_2 were calibrated once a week by reading out the digital outputs after injecting artificial input signals which simulated the real phototube signals.

The energy deposit in the calorimeter was calculated for each particle trajectory:

$$E_{cal} = \sum_i \frac{g_i Q_j}{f(x)} , \tag{7}$$

where g_j is the gain factor of the j-th phototube, Q_j is the charge from the j-th phototube, and $f(x)$ is the light attenuation along the scintillator in the x direction. Since the shower center could be predicted for each particle using the track reconstruction information, the above summation was made over the appropriate number of counters surrounding the shower center. The gain factor of each phototube was determined in the off-line analysis by minimizing

$$\chi^2 = \sum_i \left(\frac{E_{cal}(i) - E(i)}{\sqrt{E(i)}} \right)^2 , \tag{8}$$

where $E_{cal}(i)$ is the energy deposited by the i-th particle, and $E(i)$ is the energy determined by the track reconstruction.

The energy resolution could be parametrized by

$$\frac{\sigma_E}{E_{cal}} = \frac{c_1}{\sqrt{E_{cal}(\mathrm{GeV})}} . \tag{9}$$

The parameter c_1 was 0.80 for hadrons, and 0.43 for electrons. The resolution for hadrons was about consistent with what we expected [26]. However, the energy resolution for electrons was found to be degraded by the small cracks between counters. This fact could be understood as follows. The transverse development of an electron shower was much smaller than that of a hadron shower. The FWHM of a typical

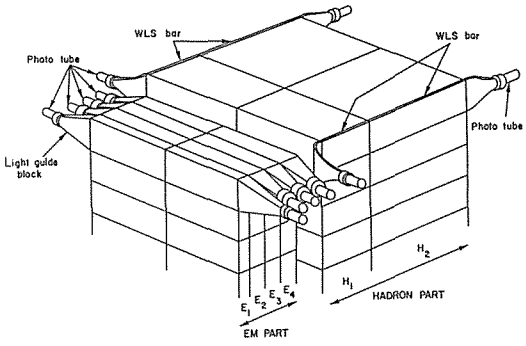

Figure 5. Schematic view of the calorimeter.

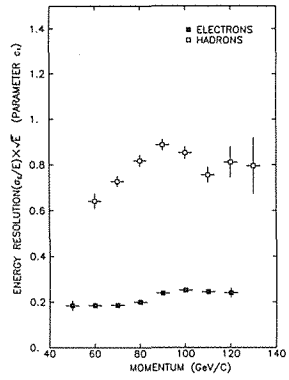

Figure 6. Momentum dependence of the energy resolution of the calorimeter.

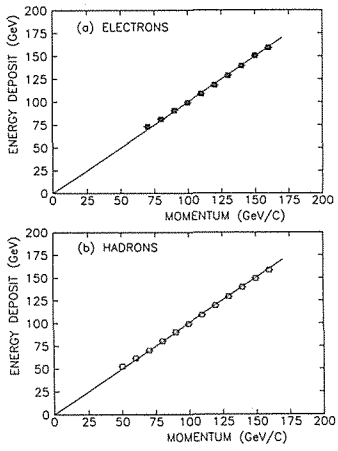

Figure 7. Linearity of the calorimeter:
(a) for electrons,
(b) for hadrons.

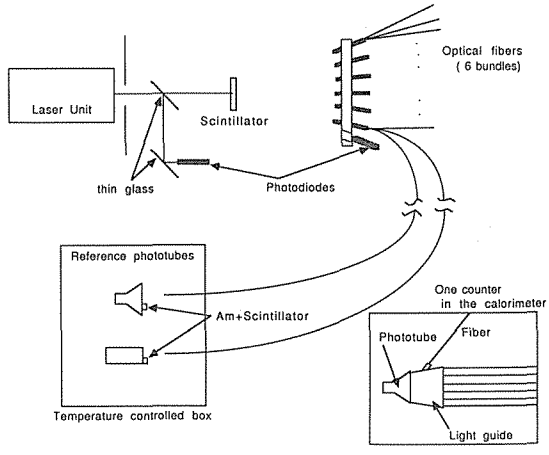

Figure 8. Schematic view of the gain monitoring system for the calorimeter.

shower was 1.3 cm for an electron shower, while it was 7 cm for a hadron shower. Therefore, an electron shower had a larger fractional energy loss in the crack than a hadron shower, if the parent particle hit near a crack. As proof, the above parameter c_1 was 0.24 for electrons which hit the center of a counter. The momentum dependence of the parameter c_1 is shown in Figure 6, and the linearity of the energy measurement in our calorimeter is shown in Figure 7.

II-8. Gain Monitor for Calorimeter

During the data acquisition, the gain of each phototube in the calorimeter was monitored by a nitrogen laser system as shown in Figure 8. The PRALN100 laser unit was employed for this system [28]. This laser unit emitted fast ultraviolet laser pulses at 337.1 nanometer wave length. The pulse duration was 300 picoseconds. The fast laser pulses were directed onto a small piece of the plastic scintillator placed about 10 cm before the laser source. This scintillator was the same kind as was used in the

calorimeter. The scintillation light fired by the laser was divided and transported to the phototubes of the calorimeter through quartz optical fibers. The fibers were divided into six bundles. Each bundle had thirty fibers. The inlet of each bundle was mounted on a spherical metal piece the radius of which was 15 cm. The scintillator was placed at the focus of the sphere so that all the fibers could receive the scintillation light identically. The outlet of each fiber was fixed on the light guide of each phototube.

The stability of this laser itself was about 5%. However, better accuracy was obtained by measuring the laser intensity pulse by pulse with stable reference counters. Two reference phototubes (Hamamatsu R1565 and R329) and two pin silicon photodiodes (Hamamatsu S1722-02) were employed as the reference counters. The reference phototubes were placed in the temperature controlled box to stabilize their gains. The scintillation light fired by the laser was sent to each reference phototube through an optical fiber. The gain of each reference phototube was monitored by a small light source attached to the surface of the phototube. This light source consisted of the americium α-ray source on a small plastic scintillator. On the other hand, the temperature dependence of the pin silicon photodiodes was 0.1 %/°C, according to the catalogue [29]. This permitted us to leave the photodiodes at room temperature. One of the photodiodes looked at the scintillator illuminated by the laser, and the other one looked at the laser light reflected by thin glass plates.

The laser was operated at 10 Hz for 1 second just after each spill. During this 1 second, the signals from the phototubes of the calorimeter were read out together with the signals from the reference counters. The accuracy of this monitoring system was evaluated by the ratio of a reference counter to another reference counter. The fluctuation of this ratio was about 3 % during the three months' operation.

III. DATA ACQUISITION

III-1. Triggers

III-1-1. Hodoscope Logic

Signals from the hodoscope counters, if they exceeded a preset discriminator threshold, were synchronized to the accelerator RF sighals by pulse stretcher modules. Then, the outputs of the pulse stretchers were sent to three places: the matrix modules, the multiplicity units, and the coincidence registers. The matrix modules and the multiplicity units generated various trigger signals as described below, while the coincidence registers latched the pattern of the hodoscope hits and sent the information to the data readout system.

The matrix modules consist of lookup tables in ECL RAM's. The lookup tables contain the possible combinations of the hodoscope counters which should be fired by the charged particle tracks coming from the target through the aperture of the SM12 magnet [30]. The matrix modules compared the hodoscope hit pattern with the stored matrix pattern in the RAM's, and generated a signal if the matrix was satisfied.

Four Y matrices YUL, YUR, YDL, and YDR were created for electrons and hadrons. These matrices specified the combinations of 3 fold coincidences for the Y1, Y2, and Y3 hodoscope counters. U(D) corresponds to the aperture above (below) the

beam dump in SM12, while L (R) corresponds to the left (right) half of the aperture. Four μ matrices μUL, μUR, μDL, μDR were created for muons. The μ matrices specified the combinations of 3 fold coincidences for the Y1, Y2, and Y4 hodoscopes. The signals coming from these matrices were combined into the following outputs.

1. For electrons and hadrons,
   YU = YUL .or. YUR,
   YD = YDL .or. YDR,
   Y = YU .or. YD,
   2Y = YU .and. YD.
2. For muons,
   μU = μUL .or. μUR,
   μD = μDL .or. μDR,
   μL = μUL .or. μDL,
   μR = μUR .or. μDR,
   μ(L+R) = μL .or. μR.

The hodoscope signals were fed into terminator modules after the matrix modules. The terminator modules performed a logical OR on the signals within a half (left or right) plane of each hodoscope. The outputs of the terminator modules were reduced to the following four signals.

1. For electron and hadrons,
   3/4L,
   3/4R.
2. For muons,
   4/4μL,
   4/4μR.

3/4L or 3/4R was a majority logic coincidence of any three planes out of the X1, Y2, X3, and Y3 hodoscopes within the corresponding left or right half planes. 4/4μL or 4/4μR was a 4 fold coincidence of the Y2, X3, Y3, and Y4 hodoscopes within the corresponding left or right half planes.

On the other hand, when the multiplicity units (LeCroy 390a) received the outputs of the pulse stretchers, they generated:

1. a veto signal called $\overline{\text{NX3}}$, if more than 10 counters in the X3 hodoscope fired in the event,
2. a signal called 2X4, if more than 2 counters in the X4 hodoscope fired.

$\overline{\text{NX3}}$ was based on the assumption that clean single or pair events would not fire very many counters at Station 3. 2X4 was used in the logic for the dimuon trigger.

III-1-2. Calorimeter Logic

The dynode signal of each phototube in the calorimeter was sent to the calorimeter logic to produce the fast trigger signals for hadrons and electrons. First of all, the dynode pulse heights were summed in weighted analog mixers (LeCroy 628) in various combinations and with appropriate weights. Figure 9 shows the combinations and the weights for the left half of the calorimeter. The right half was exactly symmetric with the left half. The weights were determined module by module so as to make the

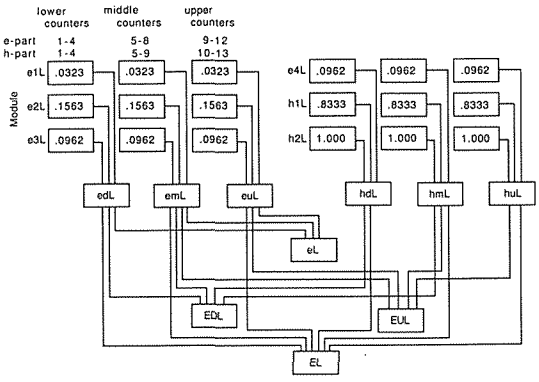

Figure 9. Left half of the calorimeter logic. The right half is exactly symmetric to the left half. The values written in the boxes are the weights for the signals.

relation between the deposited energy and the pulse height uniform over all the counters in the calorimeter. The following analog signals were created.

eL or eR: Sum of the segments in the left or right half of E1, E2, and E3.

EL or ER: Sum of all the segments in the left or right half.

EUL or EUR: Sum of the upper 8 segments in the left or right half of the EM part and the upper 7 segments in the left or right half of the hadronic part.

EDL or EDR: Sum of the lower 8 segments in the left or right half of the EM part and the lower 7 segments in the left or right half of the hadronic part.

The above analog signals were combined further, and sent to discriminators (LeCroy Model 825). The discriminators changed the analog signals into logical signals. The threshold were adjusted appropriately by attenuating the pulse heights before the discriminators. The following are the logical signals created at this stage. The procedures to create them are also given.

elo: The signals eL and eR were summed and discriminated.

e: The signals eL and eR were summed, attenuated by 3 db, and discriminated.

ETFI: EL and ER were summed and discriminated.

EHI: EL and ER were summed, attenuated by 8 db, and discriminated.

EU: EUL and EUR were separately attenuated by 10 db and discriminated. After that, a logical OR was performed on the discriminator outputs.

ED: Same operations as in EU were performed on EDL and EDR.

EL: The analog signal EL was attenuated by 3db and discriminated.

ER: The analog signal ER was attenuated by 3db and discriminated.

Indeed, both ETFI and EHI corresponded to the sum of all the segments in the calorimeter, but they had energy thresholds differing by 8 db. These dignals were used to produce the hadron trigger signals. On the other hand, elo and e corresponded to the sum of all the segments within E1, E2, and E3 in the EM part with energy thresholds differing by 3 db. Thus, elo and e participated in the electron trigger logic. Having two different threshold values was necessary to investigate the trigger efficiency near threshold.

III-1-3. DC Logic

The outputs of the hodoscope logic and the calorimeter logic were sent to two

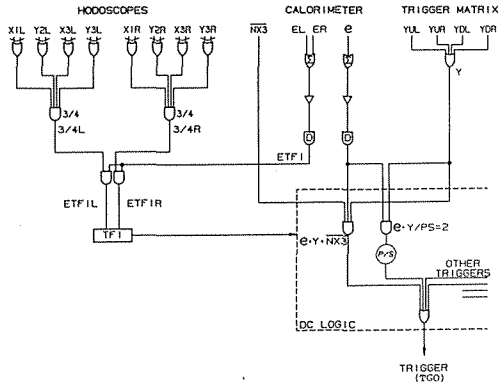

Figure 10. DC logic for electrons.

places which we called the TFI module (Trigger Fan In) and the DC logic. The DC logic performed various higher level logical operations on its inputs. The OR of the DC logic operations produced the final trigger. The schematic diagram of the DC logic for electrons is given in Figure 10.

The TFI module generated a gate signal for the DC logic when any one of the inputs to the TFI module was logically true. The following signals were the inputs to the TFI module.

1. For electrons and hadrons,
   ETFIL=3/4L · ETFI,
   ETFIR=3/4R · ETFI.
2. For muons,
   2X4 · RF,
   4/4μL/ps=8K (ps=pre-scale value),
   4/4μR/ps=8K.
3. For monitoring,
   Calib.

The symbol RF means an accelerator RF signal. The Calib pulse came from the reference phototubes in the monitor system for the calorimeter described in the previous chapter.

When the DC logic received the gate signal from the TFI module, it latched the signals sent from the hodoscope logic and the calorimeter logic onto the DC logic bus. Then, the DC logic judged whether various logical combinations of the inputs were true or false. The logic operations are summarized in Table 4. When at least one logic operation was satisfied, the DC logic commanded the TGO module (Trigger Generator Output) to generate a final trigger signal to the readout system. The TFI inputs, DC logic inputs, and DC logic outputs were latched in coincidence registers and written on the data tape.

The following logical combinations in the DC logic were used to define electron events:

e · Y · $\overline{\text{NX3}}$,
e · Y/ps=2,
elo · μ(L+R).

Table 4 Summary of the DC logic.

1. For hadrons:	
EYU, EYD,	EHI·2Y·$\overline{\text{NX3}}$, EHI·Y/ps=64,
EL·ER,	ETFI/ps=512.
2. For electrons:	
e·Y·$\overline{\text{NX3}}$,	e·Y/ps=2.
3. For eμ pairs:	
e·Y·$\overline{\text{NX3}}$,	e·Y/ps=2.
4. For muons:	
μU·μD·2X4·$\overline{\text{NX3}}$,	μL·μR,
μU·μD·2X4·$\overline{\text{NX3}}$,	4/4μL, 4/4μR,
5. For monitors:	
Calib,	elo·μ(L+R)$_{\text{delay}}$·Y.

Thus, e · Y · $\overline{\text{NX3}}$ required three conditions: adequate energy deposit in the first three modules of the EM part in the calorimeter, at least one Y matrix, and a multiplicity less than 10 at the X3 hodoscope. This logic was satisfied by single electron events and electron pair events. On the other hand, electron-muon pairs were recorded using elo · μ(L+R) which required two conditions: energy deposit in the first three modules of the EM part in the calorimeter and at least one μ matrix. The pre-scaled logic e · Y/ps=2 enabled us to obtain the efficiency of $\overline{\text{NX3}}$.

III-2. Readout System

The Nevis Transport System [31] was employed to read out the data. The whole system was controlled by an on-line PDP-11/45 computer. To reduce the readout dead time as much as possible, the data were stored in a Mega-Memory during the spill. The Mega-Memory [32] was a memory module developed at the University of Washington. It had 4 mega bytes of memory and could store about 2000 events per spill. Then, in the interval between spills, the data stored in the Mega-Memory were written on the magnetic tape by the on-line computer.

Thus, the following data were read out, and written on the magnetic tape:

1. various scaler data including the SEM outputs and 90 degree monitor outputs etc.,
2. the coincidence register outputs to record the TFI inputs, the DC logic inputs, and the DC logic outputs,
3. other coincidence register outputs to record the hodoscope hits, the MWPC hits, and the proportional tube hits,
4. TDC outputs to record the drift times of the drift chambers,
5. ADC outputs to record the pulse heights of the counters in the calorimeter, X3 hodoscope, and Y3 hodascope,
6. ADC outputs from the Cherenkov ring-imaging photon detector.

The on-line computer sampled the data and displayed information needed to

monitor the quality of the data. Data samples were also sent to a VAX-11/780 computer where the data were analysed by the same program used in the off-line analysis.

The data on which this paper are based were recorded in May, June, and July of 1984. About 300 magnetic tapes of data including electron, muon,and hadron triggers were obtained.

IV. DATA ANALYSIS

IV-1. Track Reconstruction

The first stage of the off-line analysis was to reconstruct tracks and to make date summary tapes (DTS) of potential electron events.

Since all the events, including electron, hadron, and muon triggers were recorded on the same raw data tapes at random, the electron events were selected by searching the trigger information i.e. the DC logic outputs recorded with each event. Only the events which had e · Y · $\overline{\text{NX3}}$ or e · Y/ps=2 were picked for track reconstruction.

A track reconstraction program, JACTRACK, developed by J. Crittenden was employed [33]. First, this program searched for the tracks using the drift chambers in Station 2 and Station 3. It required that at least 4 drift chamber hits at each station were recorded on each track. At this time, the following additional cuts were made in order to avoid finding false tracks and to reduce the computing time as much as possible.

1. At Station 3, the the chamber hits inconsistent with the position of any energy cluster in the calorimeter were ignored. The energy threshold for the energy cluster was 30 GeV. Most of the muon tracks were rejected at this stage, since the typical energy deposit by a muon was less than 8 GeV.
2. At Station 2, the chamber hits inconsistent with Y2 hodoscope hits were ignored.
3. Taking into account that the magnets bent the charged particles only in vertical direction, the tracks which did not point at the target in the non-bend x-z plane were immediately abandoned.
4. The y positions at Station 2 and Station 3 had a correlation as shown in Figure 11 for the tracks coming from the target. The tracks which did not satisfy this correlation were immediately abandoned.

Next, the drift chamber tracks were extraporated toward Station 1 through the SM3 magnetic field. The straight extension in the non-bend x-z plane enabled us to predict x positions of the chamber hits in Station 1. Therefore, the MWPC's in Station 1 were searched only in the y direction at the predicted x positions. It was required that at least 3 of the 6 chambers at Station 1 had corresponding hits along each track.

Each track candidate which satisfied all the above conditions was fitted by the least squares method for a trajectory with a single deflection at the effective bend plane of the SM3 magnet. The momentum was extracted from the bend angle θ_{bend} at the effective bend plane and the p_t-kick k_t of SM3:

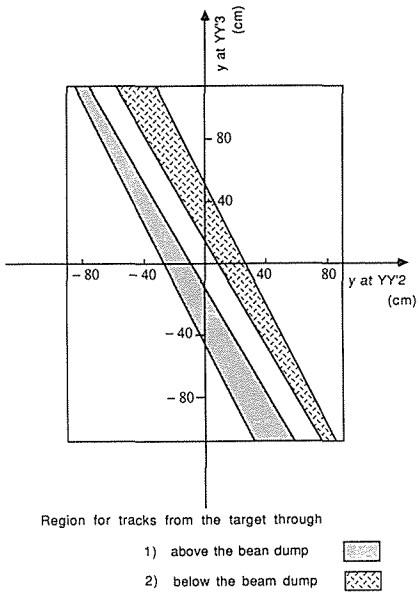

Figure 11. Correlation between the hits at Station 2 and Station 3 for the tracks from the target through the aperture of SM12.

$$p_{SM3} = \frac{k_t}{\theta_{bend}}, \tag{10}$$

where p_{SM3} was refered to as the SM3 momentum.

Thus, 40 data summary tapes (DST) were created for further analysis. These DST's had the raw data and the track information of all the electron trigger events. The track information consisted of the coordinates at the effetive bend plane of SM3, the slopes of the track before and after the bend plane, the confidence level of the fit, the chamber and hodoscope hit pattern along the track, and the SM3 momentum.

IV-2. Event Selection

From the above DST's, dielectron events were selected as described below. Eventually, 208 dielectron events were obtained. Of these events, 188 events were from the 0.508 mm thick Be target, and 20 were from the 1.016 mm thick Be target.

IV-2-1. Target-Track Requirement

First, the tracks recorded in the DST's were traced back to the target through the SM12 and SM0 magnets. In the trace-back algorithm, the SM12 and SM0 magnets were regarded as a series of 20 cm long sub-magnets, and the effective bend plane and the p_t-kick of each sub-magnet were calculated for a given track from the magnetic field map. The energy loss due to synchrotron radiation in the SM12 magnetic field was corrected at the effective bend plane of each sub-magnet. The mean energy loss ΔE(GeV) radiated in a sub-magnet is approximately given by

$$\Delta E = 0.0885 \times 10^{-3} \left(\frac{E^4}{R}\right)\left(\frac{l}{2\pi R}\right), \tag{11}$$

where E is the energy (GeV) of the electron, l is the length (m) of the sub-magnet, and

R is the radius of curvature of the electron trajectory in the sub-magnet [34]. The total energy loss due to synchrotron radiation experienced by an electron passing through SM12 magnet was typically 0.5%. This is bigger than the dielectron mass resolution in our experiment. So, correcting this energy loss is important in determining the dielectron mass.

After the trace-back to the z position of the target center ($z = -330$ cm), tracks that did not originate in the target were rejected, and events which had two opposite sign tracks of target origin were selected as dielectron candidates. Taking the accuracy of the trace-back into account, tracks that originated in the places within ± 12.7 cm of the target center both in the x direction and in the y direction were regarded as tracks of target origin.

IV-2-2. Muon and Hadron Rejections

From the dielectron candidates, muons and hadrons were rejected in the following ways.

Two planes of hodoscopes and three planes of proportional tubes placed at Station 4 were used to reject muons which deposited energy larger than 30 GeV in the EM part of the calorimeter. Extrapolating each track straight toward Station 4, the detectors at this station were searched along each track within the area allowed by multiple scattering in the calorimeter and the absorbers behind the calorimeter. The track was regarded as a muon, if it fired three or more out of the five Station 4 detectors.

To reject hadrons, the calorimeter and the Y3 hodoscope were used. Each track was extraporated to the calorimeter; there the cluster of energy deposited by each track was determined. Then, for each energy cluster, the ratio of the energy deposited in the EM part to the total energy deposited in the cluster was calculated. This ratio was refered to as the EM fraction. Since an electron deposits almost all its energy in the EM part, the EM fraction associated with an electron track is expected to be close to 1, while a hadron track is expected to have a value close to 0. The distribution of the EM fraction is shown in Figure 12 for the positive and negative sign tracks in the events surviving at this stage. A clear electron peak can be seen where the EM fraction is larger than 0.94. The tracks which had an EM fraction less than 0.94 were rejected. After that, the momentum of each track was compared with the corresponding energy deposit in the calorimeter. The solid line in Figure 13 shows the distribution of

$$R_{E/p} = \frac{E_{cal} - p_{SM3}}{\sqrt{p_{SM3}}}, \tag{12}$$

where p_{SM3} is the SM3 momentum and E_{cal} is the energy deposit in the calorimeter. Since all tracks had values between -3.2 and $+3.2$, no cut was made on this distribution.

As was mentioned in Chaper II, electrons gave bigger pulse heights to the counters in the Y3 hodoscope because of the lead sheet between the X3 and Y3 hodoscopes. Therefore, the pulse height in the Y3 hodoscope counter was used as additional information to identify the particle. The position where each track hit the hodoscope plane was calculated, and only the pulse height from the counter which was hit by each

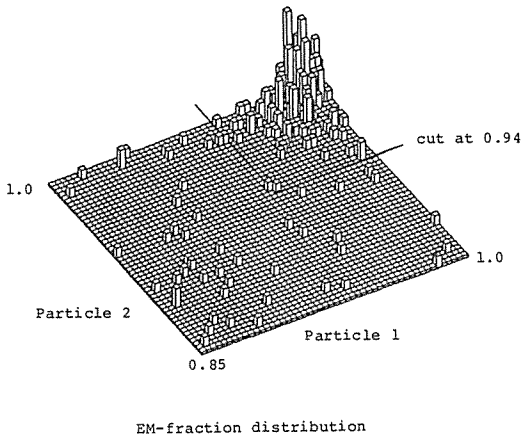

Figure 12. EM fraction distribution for the positive and negative sign tracks in the dielectron candidates. Of the two tracks in each event, the track which has a higher confidence level is denoted by Particle 1. Particle 2 is the track which has a lower confidence level.

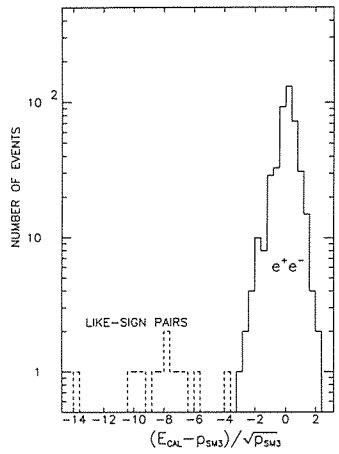

Figure 13. Distribution of $(E_{cal}-p_{SM3})/\sqrt{p_{SM3}}$ of opposite-sign electron pair candidates(solid line). The dashed line is the same distribution of the like-sign electron pairs.

track was used. Figure 14(a) shows the pulse height distribution of the dielectron candidates which survived the above EM fraction cut. On the other hand, Figure 14(b) shows the same distribution of hadrons which were selected by requiring an EM fraction less than 0.1. Comparison of these two figures suggests a cut at 10 picocoulombs. Thus, the tracks which had pulse height less than 10 picocoulombs were rejected from the dielectron candidates.

IV-2-3. Trigger Matrix Requirement

In the trigger logic for electrons, at least one trigger matrix was required. However, at the trigger stage, the matrix might be satisfied not by the electron track but by other random background hits. So, in the off-line analysis, the hodoscope hit pattern along each track was compared with the matrices which were actually used in the data acquisition, and we required that one of the two tracks in each event satisfy at least one trigger matrix combination.

IV-2-4. Fiducial Cuts

Fiducial cuts related to the geometry of our apparatus were applied for the convenience in making corrections needed to extract the cross section of dielectron production. The purpose of the fiducial cuts are rejecting events which hit inefficient regions of the apparatus.

Owing to the transverse spread of the electromagnetic shower in the calorimeter, the electron lost some of its energy outside the calorimeter, if it hit near the edge of the calorimeter. Since such events decreased the trigger efficiency, tracks which hit within

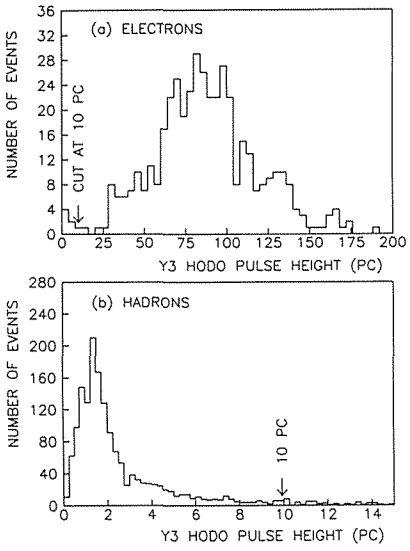

Figure 14. Pulse height distribution of Y3 hodoscope:
(a) for the electron candidates,
(b) for hadrons.

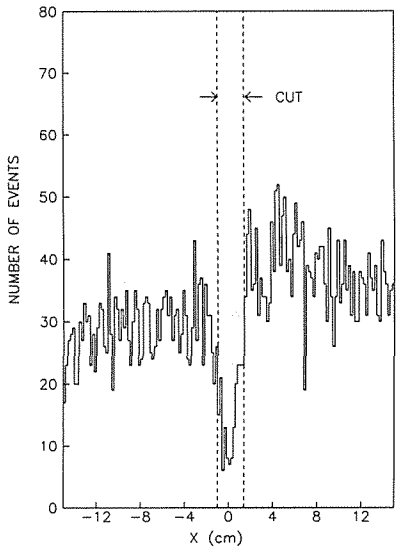

Figure 15. The x position distribution of single electrons at the E3 module of the calorimeter.

2.5 cm of the calorimeter edge were rejected. This cut guaranteed that the energy leakage was less than 10%.

Another fiducial cut was made to avoid the inefficient region at the boundary between the left and right halves of our apparatus. This inefficient region was determined by investigating the position distribution of the single electron events aquired using the same triggers as the dielectrons. The reason why single electron events were chosen for this purpose was just to obtain better statistical accuracy. Figure 15 shows the x position distribution of those electron tracks at the E3 module of the calorimeter. The central region at this module,

$$-1.0\ \text{cm} < x < 1.4\ \text{cm}\,,$$

was rejected, because a rapid decrease in yield could be seen in this region.

Fiducial cuts were also applied at the collimators and the beam dump in the SM12 and SM0 magnets and at the Y3 hodoscope in Station 3. These cuts are listed in Table 5 together with the above cuts at the calorimeter. The cuts in the SM12 and SM0 magnets were actually made for the trajectories which were constrained to the target center in the way as described in the next section.

Finally, 208 dielectron events were selected.

IV-3. Determination of Observales

When the tracks were traced back to the target using the momenta measured by the SM3 magnet, the distribution of the apparent target position was much broader than the actual target thickness due to the finite error of the SM3 momentum. The y position distribution at the target is given in Figure 16.

Table 5 Fiducial cuts.
(Tracks passing through the x and y regions given below were accepted.)

	z(cm)	y range(cm)	x range(cm)
Collimator (Downstream edge)	−26.7	$-24.1 \leqq y \leqq -11.4$ or $11.2 \leqq y \leqq 23.4$	——
Dump	264.1	$-41.9 \leqq y \leqq -19.5$ or $18.3 \leqq y \leqq 41,1$	——
Dump (Downstream edge)	767.1	$-52.6 \leqq y \leqq -19.8$ or $20.6 \leqq y \leqq 51.8$	——
Y3 hodo	4691.9	$-114.6 \leqq y \leqq 119.1$	——
Calorimeter (E3 module)	4724.5	$-119.4 \leqq y \leqq 119.4$	$-117.7 \leqq x \leqq -1.0$ or $1.4 \leqq x \leqq 115.0$

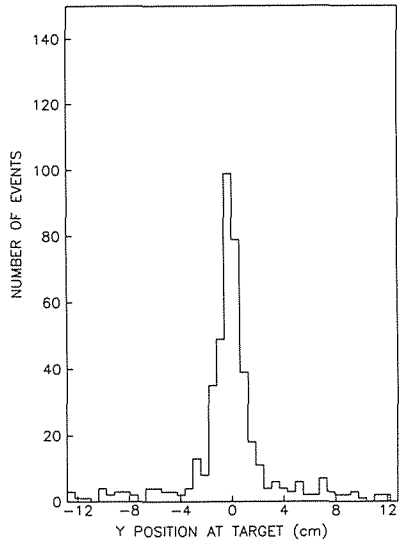

Figure 16. The y position distribution at the z coordinate of the target center. Only the electron tracks in the dielectron events were used.

The momentum of each track was re-evaluated using the SM12 magnet by constraining the track to the target center in the vertical y–z plane. This momentum was refered to as the SM12 momentum. Since SM12 had a larger p_t-kick than SM3, the SM12 momentum was more accurate. The production angle of each particle was also re-evaluated from the trajectory after constraining to the target center.

The SM12 momentum was obtained by iterating the trace-back and modifying the SM3 momentum until the y position of the trajectory matched the target center. Modifying the SM3 momentum included not only modifying the absolute value but also adjusting the bend angle at the SM3 bend plane in accordance with the modification. Taking into account the fact that the predision of the SM3 momentum was restricted by the poor spatial resolution of the MWPC's at Station 1 and the relatively short distance between Station 1 and the SM3 bend plane, the bend angle adjustment was made for the trajectory upstream of the SM3 bend plane; the downstream trajectory was not altered. The quantitative discussion on the resolution is described later.

After the event selection described in the previous section, the invariant mass of a

given dielectron event was calculated using the SM12 momenta. The invariant mass was given gy

$$M = \sqrt{2p_{e^+}p_{e^-}(1-\cos\theta_{open})}\,, \tag{13}$$

where p_{e^+} or p_{e^-} is the momentum of e^+ or e^-, and θ_{open} is the opening angle between the two momenta. The transverse momentum of the dielectron was given by

$$p_t = \sqrt{(p_{e^+x}+p_{e^-x})^2+(p_{e^+y}+p_{e^-y})^2}\,, \tag{14}$$

where the subscript x or y indicates the x or y component of the momentum.

The rapedity y were calculated according to the formulas defined in Chapter 1. The decay angle of the dilepton is defined as the angle between the incoming quark and outgoing lepton in the dilepton rest frame. However, the direction of the incoming quark is uncertain because of the intrinsic transverse motion of the quark. Instead, the beam direction was used as the axis from which the decay angle was measured. This is known as the Gottfried-Jackson frame.

IV-4. Background Estimation

Suspicious background sources were evaluated in the ways described below, and found to be negligibly small compared with the statistical error of the observed dielectron events.

IV-4-1. Accidental Coincidences

First of all, accidental coincidences of e^+ and e^- were estimated by observing like-sign pairs. A like-sign pair is an event which consists of an e^-e^- or an e^+e^+, while the dielectrons being studied can lead only to an opposite-sign pair. Electrons coming from various sources, such as gamma ray conversions or Dalitz decays etc., could mimic dielectron events by means of accidental coincidences. Such accidental coincidences would contaminate both opposite-sign pairs and like-sign pairs identically, because the apparatus was symmetric for positive and negative particles. For like-sign pairs, the major source was accidental coincidences. Therefore, the like-sign pair study gave a good estimation of the accidental coincidence rate.

Like-sign pairs were searched for in the same way as the opposite-sign pairs except for requiring two same sign tracks. There were 13 events which satisfied all the conditions except for the condition that the energy deposit in the calorimeter agree with the SM3 momentum. However, their energy deposits in the calorimeter were much smaller than the deposits which were expected from their momenta. As is shown by the dashed line in Figure 13, the distribution of

$$R_{E/p} = \frac{E_{cal}-p_{SM3}}{\sqrt{p_{SM3}}}$$

of these 13 like-sign pair candidates is far from zero, and occupies the region below that of the opposite-sign events. These 13 events have a common characteristic that both tracks in the pair hit the calorimeter near each other, and so, the energy clusters in the calorimeter completely merge. In such a case, the p_{SM3} is adopted a sum of two

momenta, and E_{cal} is an energy deposited in the merged cluster. The $R_{E/p}$ distribution of the 13 like-sign pair candidates indicates that one of the two tracks in the pair was a fake. Thus, no like-sign pairs survived the cuts.

IV-4-2. Decay Electrons

Hadron pairs or heavy lepton pairs produced in hadronic collisions could contaminate the dilepton events through their leptonic decay. This kind of background was estimated by observing eμ pairs. Assuming e-μ universality in the leptonic decays of various particles, the rate of eμ pairs due to such decays should be equal to the rate of dielectrons from the same source. The eμ pairs have been searched by R. E. Plaag (University of Wasington) [32], and only three eμ pair candidates were observed in elo · μ(L+R) trigger events.

IV-4-3. Hadron Rejection Factor

Hadron pairs could mimic dielectrons, if both hadrons were identified as electrons by mistake. In order to estimate this sort of background, the hadron rejection factor i.e. the probability for a hadron to mimic an electron was estimated by applying the conditions used for electron identification to hadrons. The events used for this purpose were the ones acquired with pre-scaled ETFI trigger which required an energy deposit larger than 60 GeV in the calorimeter and a coincidence in three planes of the X1, Y2, X3, and Y3 hodoscopes. As a matter of fact, more than 90 % of the ETFI events were hadrons, though this trigger could be fired also by electrons. The EM fraction distributions of ETFI events are shown in Figure 17(a) before and after the Y3 hodoscope cut. The Y3 hodoscope cut was made at 10 picocoulombs. The hadron peak which can be seen at an EM fraction less than o.1 has a long tail toward the electron region, and the electron peak can be seen above the tail of hadrons. While few events in the electron region are rejected by the Y3 hodoscope cut, 95% of hadrons are rejected

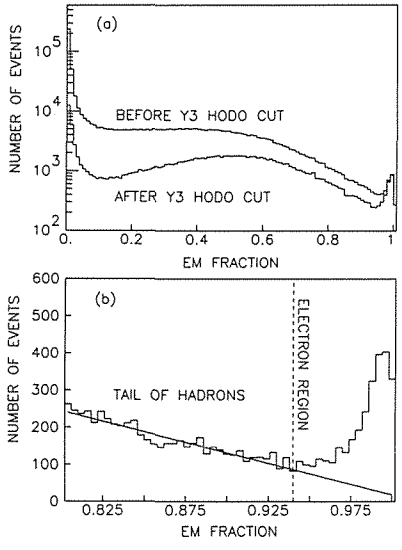

Figure 17. (a) EM fraction distribution of the events acquired with the pre-scaled ETFI trigger.
(b) The EM fraction distribution from 0.802 to 0.926 was fitted with a straight line, and was extended toward the electron resion.

by this cut. The shape of the hadron tail in the electron region was determined, as shown in Figure 17(b), by fitting the distribution from 0.802 to 0.928 with a straight line and extrapolating it toward the electron region for which the EM fraction is larger than 0.94. Then, the hadron rejection factor is given by

$$R_h = \frac{N_{em}^h}{N_{tot} - N_{em}^e}, \tag{15}$$

where N_{em}^h is the estimated number of hadrons in the electron region after Y3 hodoscope cut, N_{tot} is the number of entire events used in this analysis, and N_{em}^e is the estimated number of electrons after subtructing hadrons. The hadron rejection factor obtained in this way was 1.2×10^{-3}. This means the probability for both the hadrons in the pair to mimic electrons is $R_h^2 = 1.4\times10^{-6}$.

Angelis et al. [35] measured hadronic production of π^0 pairs, and they determined the mass spectrum of the π^0 pairs as a fucntion of $\sqrt{\tau} = m/\sqrt{s}$. Assuming their results for charged hadron pairs at $\sqrt{s} = 38.8$ GeV, the R_h^2 times hadrons pair cross section is 4×10^{-4} pb/(GeV/c^2)/nucleon at $m=8$ GeV/c^2. On the other hand, the dielectron cross section is about 5 pb/(GeV/c^2)/nucleon, which will be presented as our result later. Therefore, the contamination by hadrons is negligibly small at $m=8$ GeV/c^2. As the mass increases, the hadron pair spectrum drops more rapidly than the dielectron spectrum. So, the hadron contamination is even smaller at the higher mass.

IV-5. Monte Carlo Simulation

The Monte Carlo method was useful to understand the measurement resolution of various observables and to calculate the acceptance of our apparatus. The CERN software package GEANT [36] was used to simulate the experimental apparatus and generate imitaion events. The events generated by the Monte Carlo method were transformed into a data set in the same format as the real data. Thus, the same program as was used to analyze the real data could also analyze the Monte Carlo events. This method enabled us to estimate not only the geometrical acceptance but also the acceptance with various corrections included. In order to make maximum use of this technique, all known effects were simulated, such as multiple scattering, electron bremsstrahlung, energy loss due to ionization, radiative corrections, the spatial resolution of the drift chambers, the efficiencies of the hodoscope counters and wire chambers, background hits at Station 3 chambers, and synchrotron radiation in the magnets.

IV-5-1. Electromagnetic Effects

There are two different types of electromagnetic effects which can deteriorate the measurement resolution:

1. interactions of the electron with the materials in our apparatus, such as multiple scattering, electron bremsstrahlung, and energy loss due to ionization,
2. radiative corrections to the decay of a massive virtual photon into a lepton pair.

The former were generated by the standard routines in GEANT.

The latter i.e. radiative corrections due to the emission of photons near the vertex of the lepton pair modify the shape of the dilepton mass spetrum [37]. If virtual photons of an invariant mass M_0 are produced with a rate W_0 and decay into lepton pairs, the dilepton mass spectrum due to hard photon emission is written as

$$\frac{\mathrm{d}W_h}{\mathrm{d}M^2} = \frac{W_0}{M_0^2}\frac{\alpha}{\pi}\frac{1+z^2}{1-z}\left\{\ln\left(\frac{M^2}{\mu^2}\right)-1\right\}, \tag{16}$$

where M is the observed dilepton mass, μ is the lepton mass, and $z \equiv M^2/M_0^2$. The hard photon is a photon which has an energy larger than the experimental energy resolution ω_s. The mass spectrum due to soft photon emission is written as

$$\frac{\mathrm{d}W_s}{\mathrm{d}M^2} = W_0(1+d_s)\,\delta(M_0^2-M^2), \tag{17}$$

where

$$d_s = -\frac{\alpha}{\pi}\left[2\left\{\ln\left(\frac{M_0}{2\omega_s}\right)-\frac{3}{4}\right\}\left\{\ln\left(\frac{M_0^2}{\mu^2}\right)-1\right\}+\frac{1}{2}-\frac{\pi^2}{3}\right]. \tag{18}$$

Thus, for given virtual photon invariant mass M_0, the dielectron mass after radiative corrections was simulated using the above formulas in the Monte Carlo calculation.

IV-5-2. Spatial Resolution

The spatial resolution of each drift chamber was estimated, using the reconstructed tracks in real events, by the method of measuring the residual distance between the point determined by a given chamber and the trajectory reconstructed by the least squares fit. The typical resolution of the drift chambers in Station 2 and Station 3 was 0.22 mm.

IV-5-3. Counter and Chamber Efficiencies

The efficiencies of the hodoscope counters were estimated using events acquired with the pre-scaled ETFI trigger, because those events were free of the trigger matrix requirement. The efficiency ϵ_{ij} of the i-th counter in the j-th hodoscope plane was determined by

$$\epsilon_{ij} = \frac{N_{i0}}{N_{i0}+N_{ij}}, \tag{19}$$

where N_{i0} was the number of the tracks which penetrated i-th counter in the j-th plane and fired all the counters along the tracks, N_{ij} was the number of the tracks which penetrated i-th counter in the j-th plane but failed to fire this counter. Most of the counter efficiencies were more than 95%.

The wire chamber efficiency was estimated in the same way. There were so many wires that measuring the efficiency wire by wire was not realistic. Therefore, the wires in each chamber were grouped into four segments, and a efficiency was determined for each segment. The average efficiency of the MWPC's at Station 1 was 88%, and that of the drift chambers at Station 2 and Station 3 was 94%.

In GEANT, hits on hodoscope counters and wire chambers were generated along each trajectory so as to reproduce the measured efficiencies.

IV-5-4. Background Hits at Station 3

As was noted in Chapter II, the Cherenkov counter placed between Station 2 and Station 3 had 0.21 radiation lenghts of material, including the gas vessel and the mirrors placed in the vessel. This amount of material was not negligible for electrons. After an electron traversed these media, it might be accompanied by other electrons or gamma rays created in the material. If this was the case, the companion photons and electrons could degrade the resolution in position measurement, or they might even reduce the track reconstruction efficiency.

Since GEANT was not suitable for generating such background particles, the SLAC software package EGS was used instead of GEANT. The EGS program was originally written to simulate electromagnetic showers, but it can be used to simulate all the electromagnetic effects [38]. 30,000 electrons with 100 GeV energy were generated from the entrance of Cherenkov counter toward Station 3, and the electrons which arrived at Station 3 chambers were recorded. The multiplicity distribution of the background at the U chambers in Station 3 is given in Figure 18(a). 87.5% of the events had no background hit, 2.7% had one additional charged track, 8.8% had two, etc. The dominance of multiplicity 2 over multiplicity 1 can be explained by electron bremsstrahlung which subsequently produces an electron pair. The distribution of the background hits at the U chambers in Station 3 is given in Figure 18(b). The x axis is the distance (cm) between the incident electron and its companion at the U chambers in Station 3. This distribution was fitted with a sum of two exponentials:

$$f(x) = A_1 e^{-x/l_1} + A_2 e^{-x/l_2}, \tag{20}$$

where

$$(A_1,\ l_1) = (1.96\times10^3,\ 0.132),$$
$$(A_2,\ l_2) = (1.16\times10^2,\ 2.64).$$

Using these results obtained by the EGS, background hits were generated near each electron trajectory at Station 3 in GEANT.

IV-5-5. Synchrotron Radiation

As was mentioned in Section IV-2-1, the mean value of the synchrotron radiation energy loss in the SM12 magnet was corrected in the data analysis. In GEANT, synchrotron radiation was treated as a discrete process in order to reproduce the fluctuations of the energy loss. The number of photons radiated in a sub-magnet of SM12 is described as a function of the photon energy by

$$\frac{dN}{d\epsilon} = \frac{l}{2\pi R}\frac{\alpha\gamma}{\epsilon}F\left(\frac{\omega}{\omega_c}\right), \tag{21}$$

where R is the radius of curvature of the electron trajectory, l is the length of the sub-magnet, ω is the frequency of the photon, ω_c is the critical frequency of the

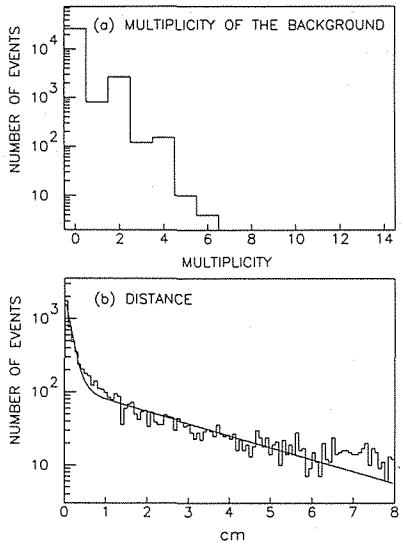

Figure 18. Simulation for the backgrounds at Station 3:
(a) Multiplicity of the background hits at the U chambers in Station 3.
(b) Distribution of the background hits at the U chambers in Station 3. The x axis is the distance (cm) between the incident electron and its companion electrons.

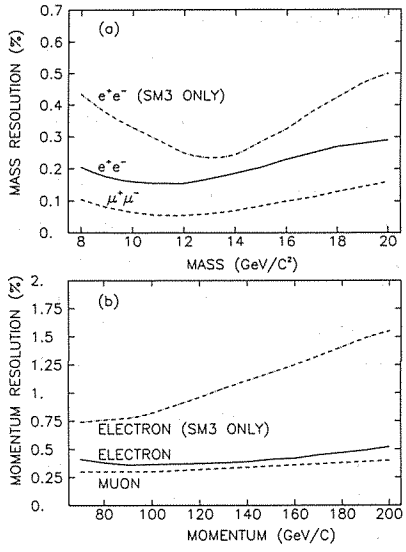

Figure 19. Resolution:
(a) Mass resolution as a function of mass. The solid line is for dielectrons, the dashed line for dimuons, and the dashed-dotted line for dielectrons analized with SM3 momenta.
(b) Momentum resolution as a function of momentum. The solid line is for electrons, the dashed line for muons, and the dashed-dotted line for electrons analized with SM3 momenta.

synchrotron radiation, and ϵ is the photon energy $\hbar\omega$ [39]. $F(y)$ is the function

$$F(y) = 2\sqrt{3}\, y \int_{2y}^{\infty} K_{5/3}(x)\mathrm{d}x\,, \tag{22}$$

where $K_{5/3}(x)$ is a modified spherical Bessel function of the second kind. The critical frequency of the synchrotron radiation is

$$\omega_c = \frac{3\gamma^3 c}{R}\,. \tag{23}$$

Following this formula, synchrotron radiation was simulated for each electron trajectory in SM12.

IV-6. Resolution

The measurement resolution of various kinematical variables was studied by the Monte Carlo method decribed in the previous section. The calculated dilepton mass resolution is given in Figure 19(a) as a function of the dilepton mass. The solid line is

the dielectron mass resolution using the SM12 momenta. The expected mass resolution at the $\Upsilon(9.46\,\mathrm{GeV/c^2})$ is 0.17 %. The resolution using the SM3 momenta (the dotted-dashed line) is worse by a factor of 2 at the Υ mass. The dimuon mass resolution given by the dashed line is better than that of dielectrons by a factor of 2, because dimuons are free from synchrotron radiation, bremsstrahlung, and the extra hits at Station 3 chambers. The lack of synchrotron radiation makes the biggest contribution in improving the dimuon mass resolution. The momentum resolution is also given in Figure 19(b) as a function of the momentum.

Next, the Υ family of resonances were simulated to investigate how they looked in our apparatus. The simulated dielectron mass spectra for Υ, Υ', and Υ'' are presented in Figure 20. The masses used in the Monte Carlo method were

$$(M_{\Upsilon},\ M_{\Upsilon'},\ M_{\Upsilon''})=(9.460,\ 10.0234,\ 10.3555)\mathrm{GeV/c^2}$$

They are the averages of the precise measurements by the e^+e^- collider experiments [40]. The intrinsic widths of these resonances were not taken into account, because they are negligibly small compared with the mass resolution of our apparatus. The measured decay widths of the Υ, Υ', and Υ'' are less than 50 KeV [41].

Each resonance shows a sharp peak, the width of which is consistent with the mass resolution. However, besides the peak, there is a low but long tail extending about 1 $\mathrm{GeV/c^2}$ below the peak. This tail is caused by radiative corrections. The shape of each simulated dielectron resonance was fitted with a sum of a function to represent the peak and a function to represent the tail:

$$F_{res}(m) = F_{peak}(m)+F_{tail}(m)\,. \tag{24}$$

Since the shape of the peak was not symmetric, a function similar to the Landau distribution was employed for the peak:

$$F_{peak}(m) = A_1\exp\left\{\frac{A_2(m-A_3)}{A_4} - \exp\left(\frac{m-A_3}{A_4}\right)\right\}. \tag{25}$$

The tail was represented by

$$F_{tail}(m) = A_5 g(m)\left[\exp\left(\frac{m-A_6}{A_8}\right)+A_9\exp\left(\frac{m-A_6}{A_{10}}\right)\right], \tag{26}$$

where

$$g(m) = \begin{cases}(A_6-m)^{A_7}, & \text{if } m\leq A_6\\ 0\quad\ , & \text{if } m>A_6\end{cases} \tag{27}$$

The fit parameters are given in Table 6. The fitted curves are superimposed on the mass spectra in Figure 20.

IV-7. Normalization

The measured cross section as a function of mass is given by

$$\frac{\mathrm{d}^2\sigma}{\mathrm{d}m\mathrm{d}y} = \frac{N_{ev}(m,\ y)}{\epsilon(m,\ y)}\,\frac{1}{LA(m,\ y)\Delta y\Delta m}\,, \tag{28}$$

Table 6 Fit parameters for each resonance

	Υ	Υ'	Υ''
A_1	4174.89	5230.44	4841.95
A_2	1.52118	1.09492	1.56640
A_3	9.45160	10.0227	10.3463
A_4	1.92404×10^{-2}	1.56606×10^{-2}	2.04841×10^{-2}
A_5	1.94773×10^{7}	2.01421×10^{5}	8.18356×10^{6}
A_6	9.60062	10.1514	10.5294
A_7	6.81991	4.45755	6.97058
A_8	6.05456×10^{-2}	9.33023×10^{-2}	7.05374×10^{-2}
A_9	1351.47	312.172	1365.44
A_{10}	2.59845×10^{-2}	3.66537×10^{-2}	3.06221×10^{-2}

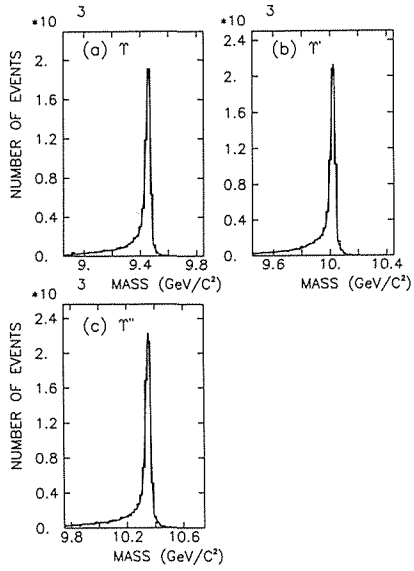

Figure 20. Mass spectra of the simulated Υ family of resonances.

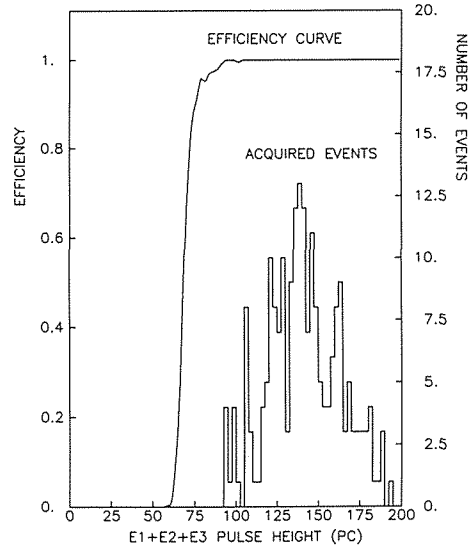

Figure 21. Efficiency of the calorimeter trigger as a function of the pulse height of the first three modules of the EM calorimeter. The same pulse height distribution of the dielectron events are superimposed.

where $N_{ev}(m, y)$ is the number of events which have masses between m and $m+\Delta m$ and rapidities between y and $y+\Delta y$, $\epsilon(m, y)$ is the overall efficiency for these events, L is the integrated luminosity, and $A(m, y)$ is the acceptance calculated by the Monte Carlo method.

The p_t distribution of the dileptons is usually written as an invariant cross section, which is written in the variables p_t and rapidity as

$$E\frac{d^3\sigma}{dp^3}=\frac{1}{\pi}\frac{d^2\sigma}{dp_t^2dy}=\frac{N_{ev}(p_t, y)}{2\pi\epsilon(p_t, y)}\frac{1}{LA(p_t, y)\overline{p_t}\Delta p_t\Delta y}, \tag{29}$$

where $\overline{p_t}$ is the mean transverse momentum of a given bin.

IV-7-1. Integrated Luminosity

The integrated luminosity is calculated by

$$L = \rho N_0 N_{inc} \int_0^l e^{-x/\lambda} dx = \rho N_0 N_{inc} \lambda (1 - e^{-l/\lambda}), \tag{30}$$

where N_{inc} is the number of incident protons, N_0 is Avogadro's number, ρ is the density of the target (g/cm^2), and λ is the absorption length of the target. The number of incident protons was measured for each spill by the secondary emission monitor (SEM). The SEM was occasionally calibrated by inserting aluminum and copper foils in the beam. Measuring the ^{24}Na produced in the copper and the ^{18}F produced in the aluminum determined the calibration constant for the SEM with approximately a 5 % systematic error. The integrated luminosities for the Be targets were:

1.09×10^{40} nucleon/cm^2 for the 0.508 mm thick Be target,

0.12×10^{40} nucleon/cm^2 for the 1.016 mm thick Be target.

IV-7-2. Efficiency

The overall efficiency is the product of various efficiencies: targeting, readout dead time, trigger, track reconstruction, and event selection cuts. The trigger efficiency consists of the efficiencies of the calorimeter, the trigger matrix, and $\overline{\text{NX3}}$. Since the efficiencies of the hodoscope counters and the wire chambers are incorporated in the Monte Carlo calculation outlined in the previous sections, the trigger matrix efficiency and the track reconstruction efficiency are already included in the acceptance. The efficiencies of most of the cuts used in event selection are also included in the calculated acceptance.

The trigger efficiency due to the calorimeter was almost 100% for the dielectrons observed by our apparatus. The calorimeter efficiency curve as a function of the pulse height from the first three modules in the EM part of the calorimeter is given in Figure 21 together with the corresponding pulse height distribution of the observed dielectron events. The correction for the trigger inefficiency resulting from the $\overline{\text{NX3}}$ requirement was made using events recorded with the pre-scaled trigger e · Y/ps=2. Since the pre-scale factor was 2, a dielectron event which had e · Y/ps=2 but no e · Y · $\overline{\text{NX3}}$ was counted as 2 events in the data analysis. The $\overline{\text{NX3}}$ efficiency was 89 %.

Readout dead time is caused by losing an event if the trigger is generated when the readout system is busy processing another event. The efficiency of the readout system was monitored by the scaler data TGI and TGI · $\overline{\text{SB}}$. While TGI · $\overline{\text{SB}}$ counted trigger only when the readout system was not busy, TGI counted everything. Therefore, the ration of TGI · $\overline{\text{SB}}$ to TGI gives the efficiency of the readout system. The typical efficiency of the readout system was 97.9%.

The ratio of 90 degree monitor counts to SEM counts determined the targeting efficiency for each spill. The relation between this ratio and the targeting efficiency was calibrated occasionally by recording the ratio while moving the target vertically through the beam. The typical targeting efficiency was 92.4% for the 0.508 mm thick Be

target, and 97.3% for the 1.016 mm thick Be target.

IV-7-3. Acceptance

The acceptance is the ratio of the number of the events accepted by the apparatus to the number of events produced. The Monte Carlo technique calculates the acceptance as a function of any kinematical variable by summing the events over all the other variables. The differential cross section in any particular variable is determined by binning and correcting the data with the appropriate acceptance. However, the acceptance in any particular variable depends on how the other variables are generated when their distributions are not yet determined experimentally. So, the acceptance correction should be iterated until the resultant distributions of all the variables agree with those assumed in the Monte Carlo calculation. In the case of our dielectron study, this iterative procedure was carried out on the mass and p_t distributions. The rapidity and decay angular distributions were generated according to the theoretical predictions or the measurements by other experiments, because the range of those variables accepted by our apparatus was too narrow to determine their shapes.

The decay angular distribution was assumed to be isotropic for the resonances, and was assumed to be

$$1+\cos^2\theta^* \tag{31}$$

for the continuum [5].

The rapidity distribution of the resonances was generated with a flat distribution from -0.5 to 0.3 [23]. This range covers all the events recorded in our experiment. For the continuum, the rapidity distribution was calculated in the framework of the Drell-Yan process, and the rapidity was generated in the Monte Carlo calculation according to the theoretical distribution. The quark distribution functions used in the

Table 7. Quark distribution functions for a proton [11, 42], (exchange u and d for a neutron).

Valence quarks:

$$u_v(x) = \frac{2}{B(\alpha, \beta+1)} x^{\alpha-1}(1-x)^{\beta},$$

$$d_v(x) = \frac{1}{B(\alpha, \beta+2)} x^{\alpha-1}(1-x)^{\beta+1}.$$

Sea quarks:

$$q_s(x) = A_s x^{-1}(1-x)^{\beta_s}$$

$B(p, q)$ is a beta function, and

$$q_s(x)=u_s(x)=\bar{u}_s(x)=d_s(x)=\bar{d}_s(x)=2s_s(x)=2\bar{s}_s(x).$$

The parameters determined by a deep inelastic neutrino scattering experiment [42] are

$$\alpha=0.51\pm0.02,\ \beta=2.8\pm0.1,$$
$$A_s=0.27,\ \beta_s=8.1\pm0.7.$$

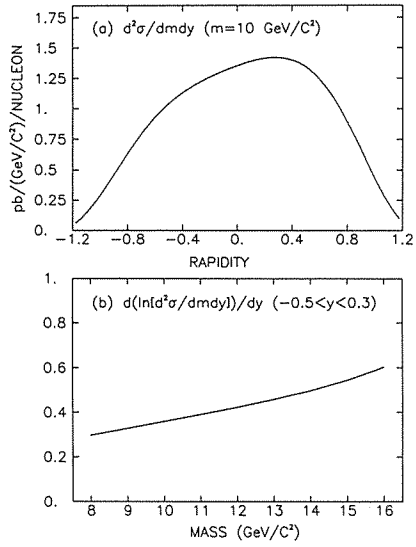

Figure 22. (a) Drell-Yan prediction for the dielectron cross section at mass 10 GeV/c^2 versus rapidity,
(b) d(ln[$d^2\sigma/dmdy$])/dy (averaged over $-0.5<y<0.3$) versus mass.

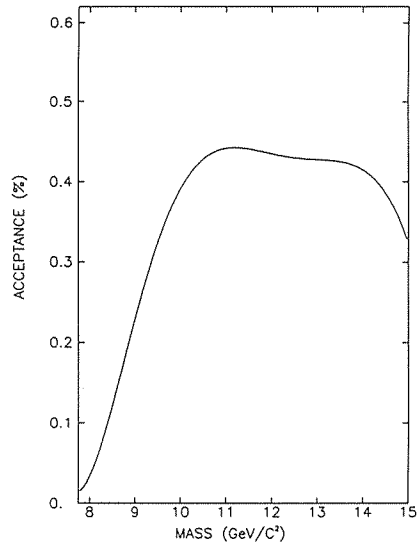

Figure 23. Acceptance versus mass for dielectron continuum.

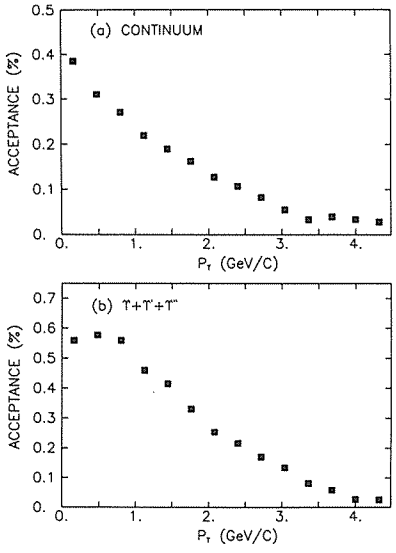

Figure 24. Acceptance versus transverse momentum:
(a) for the continuum (7.89 GeV/c^2 $\leq m<$ 14.56 GeV/c^2),
(b) for the Υ family of resonances.

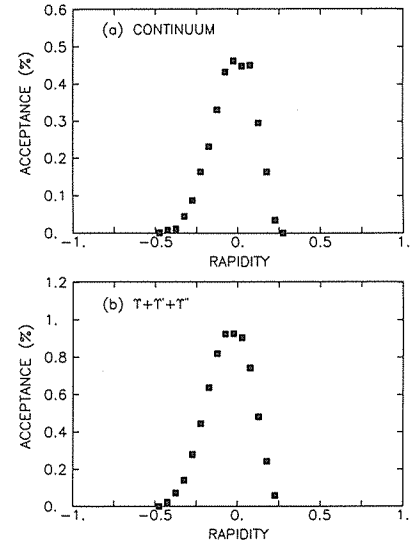

Figure 25. Acceptance versus rapidity:
(a) for the continuum (7.89 GeV/c^2 $\leq m<$ 14.56 GeV/c^2),
(b) for the Υ family of resonances.

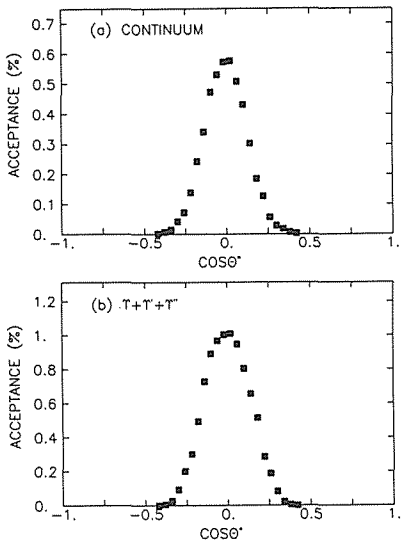

Figure 26. Acceptance versus $\cos\theta^*$:
(a) for the continuum ($7.89\ \mathrm{GeV/c^2} \leq m < 14.56\ \mathrm{GeV/c^2}$),
(b) for the Υ family of resonances.

calculation are given in Table 7. They are quark distributions based on a deep inelastic neutrino scattering experiment [11, 43]. The rapidity distribution of the Drell-Yan process in proton-berylium collisions is not symmetric about zero but has a positive slope. For example, the rapidity distribution at $m=10\ \mathrm{GeV/c^2}$ is shown in Figure 22(a). This asymmetry comes from the difference in the quark flavour distribution between the beam and the target. While there are twice as many u quarks as d quarks in the beam, the target Be nucleus contains 5 neutrons and 4 protons, and thus contains an almost even quark content of 13 u quarks and 14 d quarks. The average slope in the rapidity range from -0.5 to 0.3 is given in Figure 22(b) as a function of the dielectron mass.

The mass acceptance obtained in the above way is presented in Figure 23. The p_t rapidity, and decay angle acceptances are shown in Figure 24 to Figure 26 separately for the continuum and the resonances. The generated mass range for the continuum was from $7.89\ \mathrm{GeV/c^2}$ to $14.56\ \mathrm{GeV/c^2}$. This mass range covers all the observed events.

V. RESULTS AND DISCUSSION

V-1. Results

V-1-1. Cross Section for the Υ's

In order to count the number of the resonance events, the continuum was subtracted by fitting the raw mass spectrum with a sum of the continuum and three resonances. The continuum term was written as

$$a_1 A(m)\epsilon(m)\exp(-a_2 m)\,, \tag{32}$$

where the $A(m)$ is the mass acceptance for the continuum, and $\epsilon(m)$ is the overall efficiency at the mass m. For each resonance, the shape which was determined in Section IV-6 by the Monte Carlo method was used. For all the parameters in each

resonance shape, the values determined by the Monte Carlo method were substituted. The absolute positions of the resonances were adjusted in the fit by shifting the mass from m to $m(1+x)$. The parameter x was common to the Υ, Υ', and Υ''. Thus, the parameters which were permitted to vary in the fit were the following six: the parameters a_1 and a_2 for the continuum, the parameter x, and three parameters each of which normalized the height of each resonance. The parameter x should be consistent with zero.

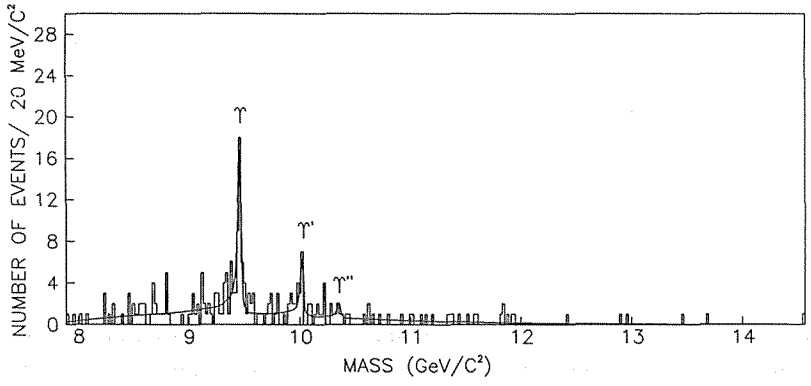

Figure 27. Raw mass spectrum of the dielectrons. The solid line is the fitted curve with a form given in the text.

The mass spectrum is presented in Figure 27 with the fitted curve superimposed on it. The parameter x was $(2.6\pm3.5)\times10^{-4}$. While the Υ can be clearly seen, the Υ'' is not clear due to the small number of the events. However, the Υ'' has been confirmed by our dimuon data acquired in 1985 [43]. After subtracting the continuum, 49, 18, and 6 events were obtained in the Υ, Υ', and Υ'' regions respectively. Those regions were defined as

$$9.31 \leq m < 9.53\ \mathrm{GeV/c^2}, \tag{33}$$
$$9.89 \leq m < 10.11\ \mathrm{GeV/c^2}, \tag{34}$$
$$10.21 \leq m < 10.43\ \mathrm{GeV/c^2}, \tag{35}$$

for the Υ, Υ', and Υ'' respectively. The mass spectrum after the continuum subtraction is given in Figure 28.

The Υ production cross section times branching ratio to decay into electron pairs is

$$B_{e^+e^-}\left(\frac{d\sigma}{dy}\right)\Bigg|_{y=-0.1}^{\Upsilon+\Upsilon'+\Upsilon''} = 2.18\pm0.35\pm0.11\ \mathrm{pb/nucleon}.$$

The first error is statistical, and the second is an uncertainty of the normalization. The ratios between the resonances are

$$\left(B_{e^+e^-}^{\Upsilon'}\frac{d\sigma}{dy}\Bigg|_{y=-0.1}^{\Upsilon'}\right)\Big/\left(B_{e^+e^-}^{\Upsilon}\frac{d\sigma}{dy}\Bigg|_{y=-0.1}^{\Upsilon}\right) = 0.32\pm0.11,$$

and

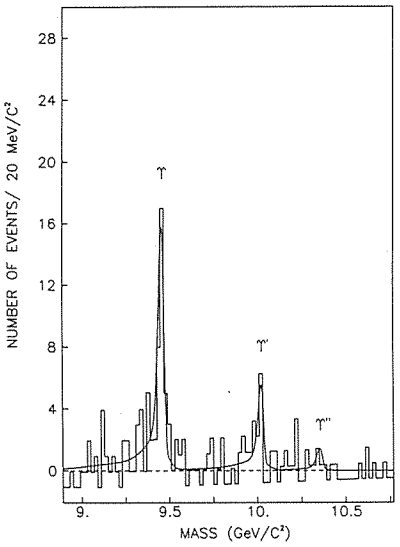

Figure 28. Mass spectrum after subtracting the continuum from Figure 29. The solid line is the fitted curve with a form given in the text.

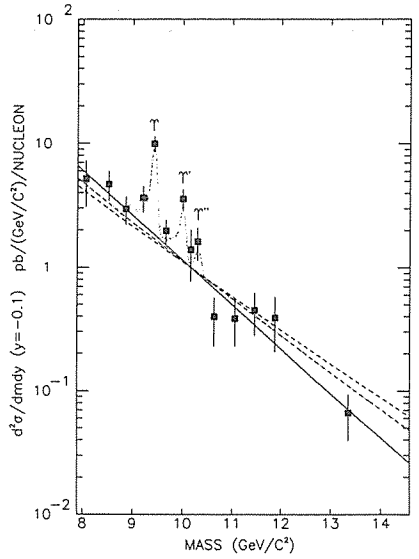

Figure 29. Dielectron differential cross section versus mass. The solid line is a exponential function fitted for the continuum. The K factor times naive Drell-Yan predictions are also superimposed. The dashed line and dashed-dotted line are associated with the quark distribution functions of Table 7 and Badier et al. [11] respectively.

$$\left(B^{r''}_{e^+e^-}\frac{d\sigma}{dy}\bigg|^{r''}_{y=-0.1}\right)\Big/\left(B^{r}_{e^+e^-}\frac{d\sigma}{dy}\bigg|^{r}_{y=-0.1}\right)=0.10\pm0.07\,.$$

V-1-2. Dielectron Continuum

After making all the necessary corrections to the raw mass spectrum, the differential cross section per nucleon was obtained as a function of mass. Figure 29 shows the dielectron differential cross section per nucleon. The data are also given in Table 8. The differential cross section was fitted with a sum of the continuum and three resonances. Again, the resonance shape obtained by the Monte Carlo method was used for each resonance. For the continuum, an exponential function was assumed:

$$\frac{d^2\sigma}{dmdy}\bigg|_{y=-0.1}=b_1\exp[-b_2(m-m_0)]\,. \tag{36}$$

A good fit was obtained with

$$b_1=1.29\pm0.13\pm0.06\ \text{pb}/(\text{GeV}/c^2)/\text{nucleon},$$

$$b_2=0.83\pm0.07\ (\text{GeV}/c^2)^{-1},$$

$$m_0=9.86\ \text{GeV}/c^2,$$

Table 8 Dielectron differential cross section versus mass

Mass Range (GeV/c^2)	Number of Events	Average Mass (GeV/c^2)	$d^2\sigma/dmdy(y=-0.1)$ (pb/(GeV/c^2)/nucleon)
7.89− 8.29	8	8.06	5.181±2.102
8.29− 8.69	21	8.52	4.694±1.254
8.69− 9.09	21	8.86	2.968±0.749
9.09− 9.31	19	9.20	3.645±0.883
* 9.31− 9.53	60	9.42	9.940±1.430
9.53− 9.89	22	9.66	1.983±0.423
** 9.89−10.11	27	10.00	3.582±0.714
10.11−10.21	5	10.16	1.396±0.624
***10.21−10.43	13	10.30	1,620±0.483
10.43−10.89	7	10.64	0.399±0.171
10.89−11.29	6	11.06	0.385±0.157
11.29−11.69	7	11.46	0.450±0.170
11.69−12.09	6	11.88	0.390±0.184
12.09−14.57	6	13.36	0.066±0.027

*Υregion; **Υ'region; ***Υ''region;

where m_0 is not a fit parameter but a parameter to minimize the correlation between the errors on b_1 and b_2.

The differential cross section was compared with the naive Drell-Yan prediction, and the K factor was extracted. Here, the K factor is defined as the ratio of the measured cross section to the cross section predicted ty the naive Drell-Yan mechanism in which no QCD correction is made. Using the quark distribution functions listed in Table 7, our data yield $K=1.87\pm0.19\pm0.09$. The error does not include the uncertainty of the quark distribution functions.

Furthermore, another set of quark distribution functions which Badier et al. determined using their dimuon mass spectrum [11] was tried. They parametrized the quark distribution in the same way as given in Table 7, and determined the parameters using their dimuon events between J/ψ and Υ. They obtained

$$\alpha = 0.5\pm0.2, \quad \beta = 3.2\pm0.4,$$
$$A_s = 0.37, \quad \beta_s = 9.4\pm1.0.$$

Using this set for our data results in $K=2.20\pm0.16\pm0.11$.

The Drell-Yan cross sections predicted with the quark distribution functions or Table 7 and Badier et al. are shown by the dashed line and the dashed-dotted line in Figure 29 respectively. They are multiplied by the K factors extracted from our data.

V-1-3. Transverse Momentum Distribution

Figure 30(a) shows the dielectron invariant cross section in the continum region versus p_t. The date are also given in Table 9(a). In order to separate the continuum from the resonances as much as possible, only the events in the continuum region were used, excluding the events in the resonance regions defined by (33), (34), and (35).

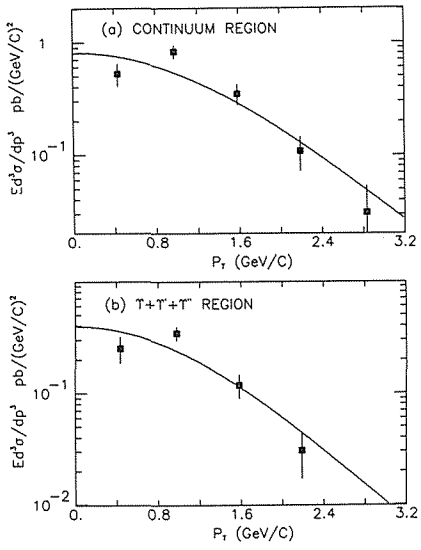

Figure 30. Invariant cross section versus transverse momentum:
(a) in the continuum region (see text),
(b) in the resonance regions (see text).

There were 126 events in the continuum region, of which 19 events were expected from the tails of the resonances, and 107 events were from the continuum. The maximum mass observed in the continuum region was 14.55 GeV/c², and the minimum was 7.89 GeV/c².

Following Kaplan et al. [6], the invariant cross section was fitted with the form

$$E\frac{\mathrm{d}^3\sigma}{\mathrm{d}p^3} = \frac{A}{[1+(p_t/p_0)^2]^6}\,. \tag{37}$$

The result was

$$A = 0.81\pm0.11\ \mathrm{pb/(GeV)^2/nucleon}\,,$$
$$p_0 = 3.66\pm0.29\ \mathrm{GeV/c}\,.$$

The mean transverse momentum $<p_t>$ calculated from the above fitting function is written as $0.430\times p_0$. Then, $<p_t>$ in the continuum region is 1.57 ± 0.12 GeV/c.

On the other hand, Figure 30(b) shows the invariant cross section in the resonance regions which were excluded from the above continuum sample. The data are also given in Table 9(b). 100 events were observed in this region, of which 73 events were expected to be the resonance events. Fitting the invariant cross section with the same form resulted in

$$A = 0.39\pm0.07\ \mathrm{pb/(GeV)^2/nucleon}\,,$$
$$p_0 = 3.30\pm0.32\ \mathrm{GeV/c}\,.$$

Then, $<p_t>$ turns out to be 1.42 ± 0.14 GeV/c.

Subtracting the contribution from the resonances in the continuum region and subtracting the contribution from the continuum in the resonance regions can determine $<p_t>$ for each of the continuum and the resonances. As a result, $<p_t>$ of the continuum is 1.61 ± 0.16 GeV/c, and that of the resonances is 1.35 ± 0.21 GeV/c.

Table 9 Invariant cross section versus p_t

(a) Continuum Region

p_t range (GeV/c)	Average p_t (GeV/c)	$Ed^3\sigma/dp^2$ (pb/GeV^2/nucleon)
0.00−0.64	0.432	0.524±0.119
0.64−1.28	0.976	0.827±0.113
1.28−1.92	1.584	0.348±0.072
1.92−2.56	2.192	0.108±0.036
2.56−3.20	2.836	0.031±0.022

(b) Resonance Region

p_t range (GeV/c)	Average p_t (GeV/c)	$Ed^3\sigma/dp^2$ (pb/GeV^2/nucleon)
0.00−0.64	0.432	0.251±0.066
0.64−1.28	0.976	0.343±0.050
1.28−1092	1.584	0.117±0.028
1.92−2.56	2.192	0.031±0.014

V-2. Discussion

One of the most remarkable features of our experiment is the improvement of the dilepton mass resolution. The mass resolution of our apparatus was 0.17% for the Υ. Compared with the previous world record achieved by the Columbia-FNAL-Stony Brook (CFS) collaboration [14], we improved the resolution by a factor of 12. From the point of view on the collision energy, we are not at the frontier, since CERN Intersecting Strage Ring (ISR) experiments measured the dielectron production at $\sqrt{s}=63$ GeV. However, because of the better resolution of our measurement, it is quite interesting to compare our results with results of other experiments or theoretical predictions.

V-2-1. *K* Factor

The measured K factors are shown in Figure 31 as a function of $\sqrt{s}$. Our result is consistent with the ones nearby. The K factor goes down from 2.4 to 1.6 as the collision energy goes up from 16.8 GeV to 62 GeV. The K factors theoretically calculated as a function of $\sqrt{s}$ are given in Figure 31 together with measured K factors. According to W. J. Stirling [44], the K factor is calculated as a function of τ and $\sqrt{s}$. For a given value of $\sqrt{s}$, the calculated K factor is flat within ±0.05 in the range $0.04<\tau<0.4$, and well approximated by

$$K \approx 1+\frac{\alpha_s(Q^2)}{2\pi}\frac{4}{3}\left(1+\frac{4\pi^2}{3}\right), \tag{38}$$

where

$$\frac{\alpha_s(Q^2)}{2\pi}=\frac{6}{33-2n_f}\frac{1}{\ln s-\ln(10\Lambda^2)}, \tag{39}$$

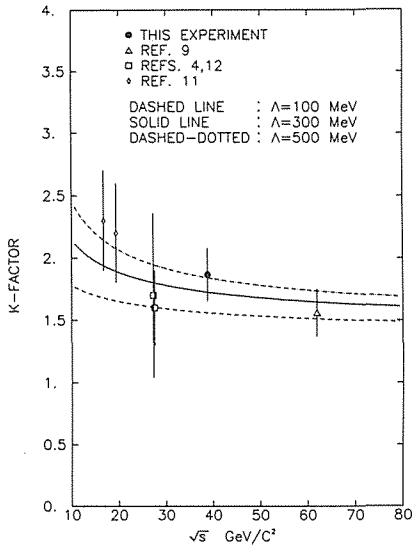

Figure 31. K factor versus $\sqrt{s}$. The dashed line, solid line, and dashed-dotted line are the theoretical predictions with Λ=100, 300, and 500 MeV respectively (see text). The circle is the data extracted from this experiment using the quark distribution functions given in Table 7. The triangle is from Ref. 9, the squares from Refs. 4, 12, and the diamond from Ref. 11.

and n_f is the number of quark flavours. The calculated K factors also decrease as $\sqrt{s}$ goes up.

V-2-2. Υ Production

Our result for the Υ production cross section times branching ratio to decay into electron pairs is shown in Figure 32 together with results of other experiments as a function of $\sqrt{\tau_\Upsilon} = M_\Upsilon/\sqrt{s}$. The cross section increases as $\sqrt{\tau_\Upsilon}$ decreases. In the theoretical prediction based on the gluon fusion model, the slope of the $\sqrt{\tau_\Upsilon}$ dependence in the Υ production cross section is derived from the shape of the gluon distribution. The data in Figure 32 were fitted with the predictions presented by V. Barger it al. [45]. They assumed for the gluon distribution

$$G(x) = \frac{1}{2}(n+1)x^{-1}(1-x)^n, \tag{40}$$

and calculated the solpes for n=5 and n=6. The normalization factor was only one parameter in the fit. The χ^2/D.F. was 6.55/8 for the slope with n=5, and 4.41/8 for the slope with n=6. A better fit was obtained with n=6.

The ratio of the resonances to the continuum

$$R_\Upsilon = \left(B_{e^+e^-}\frac{d\sigma}{dy}\Bigg|_{y=-0.1}^{\Upsilon+\Upsilon'+\Upsilon''}\right)\Big/\left(\frac{d\sigma}{dmdy}\Bigg|_{y=-0.1,m=9.46\mathrm{GeV}}^{continuum}\right) \tag{41}$$

is 1.22±0.25 GeV. This is shown in Figure 33 toghther with results of other experiments as a function of $\sqrt{\tau_\Upsilon}$. The ratio R_Υ has a smaller systematic error than the cross section itself. Comparing various data presented in Figure 33 makes us notice an inconsistency that our result at $\sqrt{\tau_\Upsilon}$=0.24 is smaller by a factor of about 1.7 than a value which can be determined by linearly interpolating other data. In determining R_Υ, the continuum subtraction to isolate the resonances is the only procedure which might

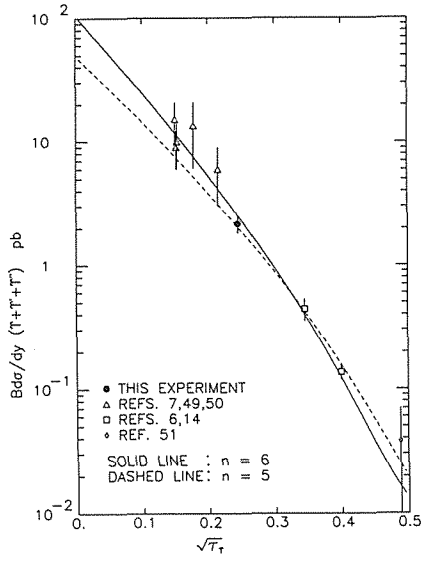

Figure 32. Cross section times branching ratio for Υ family of resonances versus $\sqrt{\tau_\Upsilon}=M_\Upsilon/\sqrt{s}$. The circle is from this experiment, the triangles from Refs. 7, 49, 50, the squares from Refs. 6, 14, and the diamond from Ref. 51. The solid line and the dashed line are the theoretical predictions by Barger et al. [45].

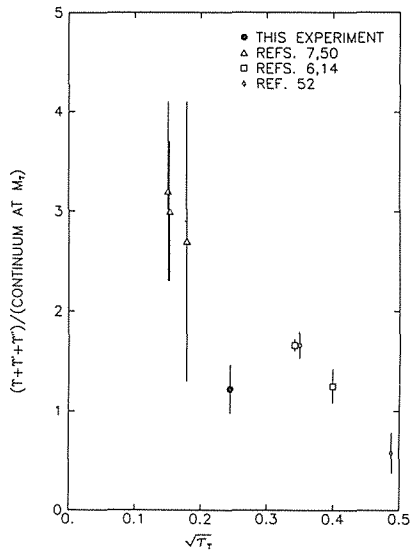

Figure 33. The ratio R_Υ defined in the text versus $\sqrt{\tau_\Upsilon}$. The circle is from this experiment, the triangles from Refs. 7, 50, and the squares from Refs. 6, 14.

cause a systematic error, and the better mass resolution makes the systematic error smaller because of the better S/N ratio. Our experiment is more advantageous in the resolution than other experiments. However, a large statistical uncertainty of our measurement prevents us from concluding that our result is more reliable than others. More data are needed to bring this problem to a firm conclusion.

Our measurements of the ratios between the yields of the Υ, Υ', and Υ'' are consistent with the results at $\sqrt{s}=27.4$ GeV presented by Ueno et al. [14]. Given the branching ratios forr the Υ, Υ', and Υ'' to decay into lepton pairs, we can extract the production ratios between Υ, Υ', and Υ'' which are not biased by a particular decay channel. Using the branching ratios measured by the e^+e^- collider experiments, our data yield

$$\left(\frac{d\sigma}{dy}\Bigg|_{y=-0.1}^{\Upsilon'}\right)\Big/\left(\frac{d\sigma}{dy}\Bigg|_{y=-0.1}^{\Upsilon}\right)=0.50\pm0.21$$

and

$$\left(\frac{d\sigma}{dy}\Bigg|_{y=-0.1}^{\Upsilon''}\right)\Big/\left(\frac{d\sigma}{dy}\Bigg|_{y=-0.1}^{\Upsilon}\right)=0.08\pm0.07\,.$$

The quoted branching ratios are

2.86 ± 0.15, 1.79 ± 0.39, 3.3 ± 1.5,

for the Υ, Υ', and Υ'' respectively. Each of these quoted values is an average of the branching ratios for each resonance to decay into e^+e^-, $\mu^+\mu^-$ and $\tau^+\tau^-$ [46]. According to the theoretical predictions presented by R. Baier and R. Ruckel [47], the production ratio of the Υ' to the Υ is less than 0.3. However, the result of our experimment rather suggest that the ratio is larger than 0.3. Taking the experimental uncertainty into consideration, the probability that this ratio is larger than 0.3 is about 83%.

V-2-3. Mean Transverse Momentum

Our result for the mean transverse momentum $<p_t>$ of the continuum is shown in Figure 34(a) together with results of other experiments as a function of $\sqrt{s}$. Only the data at $\sqrt{\tau} = m/\sqrt{s} \simeq 0.22$ were put together. Although our result was extracted from all the continuum events spreading over $0.2 < \sqrt{\tau} < 0.38$ except for the resonance regions, the mean value of $\sqrt{\tau}$ is still 0.23. As $\sqrt{s}$ goes up, $<p_t>$ of the continuum increases. This is caused by QCD effects. The theoretical prediction for $<p_t>$ of the continuum at $\sqrt{s} = 38.8$ GeV is between 1.3 GeV/c and 1.7 GeV/c when the scale constance Λ is between 100 MeV and 200 MeV [48]. This prediction agrees with our result.

The date for $<p_t>$ of the Υ family of resonances are put together in Figure 34(b). The transverse momentum of the resonances is already large at the smaller $\sqrt{s}$, and does not increase very much even if $\sqrt{s}$ goed up.

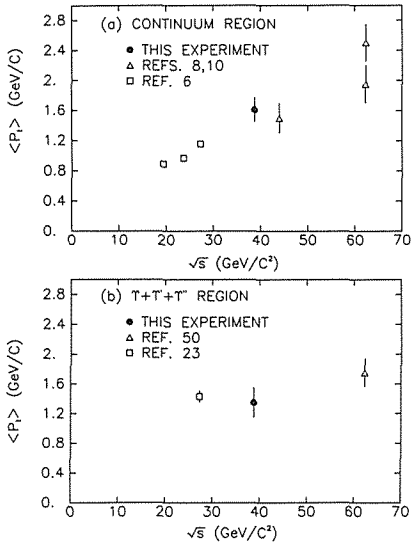

Figure 34. (a) Mean transverse momentum of the continuum versus $\sqrt{s}$. The circle is from this experiment, the triangles from Refs. 8, 10, and the squares from Ref. 6.

(b) Mean transverse momentum of the Υ family of resonances versus $\sqrt{s}$. The circle is from this experiment, the triangle from Ref. 50, and the square from Ref. 23.

V-3. Conclusion

The dielectron production at $\sqrt{s} = 38.8$ GeV was measured with a remarkably improved resolution. In conclusion, the following facts have been found:

1. The production cross section times branching ratio of the Υ family of

resonances is $2.18 \pm 0.35 \pm 0.11$ pb/nuclon.

2. A good mass resolution enabled us to measure the ratios between the Υ, Υ', and Υ''. Our measurements are consistent with the measurements at $\sqrt{s} = 27.4$ GeV. Using the available branching ratios for these resonances to to to lepton pairs, the production ratios between the resonances were extracted. The ratio of the Υ' to the Υ is 0.50 ± 0.21. The ratio of the Υ'' to the Υ is 0.08 ± 0.07.
3. The K factor, which is a ratio of the measured continuum cross section to the cross section predicted in the framework of the naive Drell-Yan process, is 1.87 to 2.20.
4. Our data indicates that the production ratio of the resonances to the continuum may be smaller than the results which were presented by other authors.
5. The mean transverse momentum $<p_t>$ is 1.61 ± 0.16 GeV/c for the continuum, and 1.35 ± 0.21 GeV/c for the Υ family of resonances. While $<p_t>$ of the continuum increases as the collision energy goes up, $<p_t>$ of the resonances does not increase so much.

Acknowledgements

It is a great pleasure to acknowledge the guidance and encouragement that I received from my advisor, Prof. K. Miyake. I would like to thank Drs. T. Nakamura, Y. Hemmi, A. Maki, N. Tamura, K. Imai, N. Sasao, and Y. Sakai for their encouragement and many useful discussions.

I would like to thank Drs. R. Gray, Y. Hsiung, D. Jaffe, R. Plaag and P. B. Straub for their helpful advices on the data analysis. I would like to thank Drs. C. Brown and J. Rutherfoord who gave me many usefuls suggestions.

A success in our experiment is owing to enormous efforts made by many people. I would like to thank each collaborator in Experiment 605: C. Brown, W. Cooper, D. Finley, A. Jonckheere, H. Jostlein, D. Kaplan, L. Lederman, S. Smith, K. Sugano, K. Ueno (Fermilab); M. Adams, H. Glass, D. Jaffe, R. McCarthy (SUNY at Stony Brook); R. Gray, K. B. Luk, R. Plaag, J. Rutherfoord, P. B. Straub, K. Young (Univ. of Washington); J. Crittenden, Y. Hsiung(Columbia Univ.); J. Hubbard, Ph.Mangeot(Saclay); F. Sauli(CERN); A. Maki(KEK); Y. Hemmi, K. Imai, K. Miyake, Y. Sakai, N. Sasao, N. Tamura(Kyoto Univ.).

Reference

1) J. H. Christenson et al., Phys. Rev. Lett. **25**, 1523 (1970).
2) D. Drell and T. M. Yan, Phys. Rev. Lett. **25**, 316 (1970).
3) I. R. Kenyon, Rep. Prog. Phys. **45**, 1261 (1982).
4) A. S. Ito et al., Phys. Rev. **D23**, 604 (1981).
5) C. Kourkoumelis et al., Phys. Lett. **91B**, 475 (1980).
6) J. K. Yoh et al., Phys. Rev. Lett. **41**, 684 (1978);
D. M. Kaplan et al., Phys. Rev. Lett. **40**, 435 (1978).

7) A. L. S.Angelis et al., Phys. Lett. **87B**, 398 (1979).
8) D. Antreasyan et al., Phys. Rev. Lett. **47**, 12 (1981).
9) D. Antreasyan et al., Phys. Rev. Lett. **48**, 302 (1982).
10) A. S. Angelis et al., Phys. Lett. **147B**, 472 (1984).
11) J. Badier et al., Phys. Lett. **89B**, 145 (1979);
J. Badier et al., Phys. Lett. **96B**, 422 (1980).
12) S. R. Smith et al., Phys. Rev. Lett. **46**, 1607 (1981).
13) G. Curci and M. Greco, Phys. Lett. **92B**, 175 (1980);
G. Curci and M. Greco, Phys. Lett. **102B**, 280 (1981).
14) K. Ueno et al., Phys. Rev. Lett. **42**, 486 (1979);
S. W. Herb et al., Phys. Rev. Lett. **39**, 252 (1977);
W. R. Innes et al., Phys. Rev. Lett. **39**, 1240 (1977).
15) Ch. Bergen et al., Phys. Lett. **76B**, 243 (1978);
C. .Darden et al., Phys. Lett. **76B**, 246 (1978).
16) J. K. Bienlen et al., Phys. Lett. **78B**, 360 (1978);
C. W. Darden et al., Phys. Lett. **78B**, 364 (1978).
17) D. Andrews et al., Phys. Rev. Lett. **44**, 1108 (1980).
18) E. Eichten and K. Gottfried, Phys. Lett. **66B**, 286 (1977);
C. Quigg and L. Rosner, Phys. Lett. **71B**, 153 (1977);
A. Martin, Phys. Lett. **93B**, 338 (1980).
19) D. Andrews et al., Phys. Rev. Lett. **45**, 219 (1980);
G. Finocchiaro et al., Phys. Rev. Lett. **45**, 222 (1980);
D. M. J. Lovelock et al., Phys. Rev. Lett. **54**, 377 (1985);
D. Besson et al., Phys. Rev. Lett. **54**, 318 (1985).
20) K. an et al., Phys. Lett. **49**, 1612 (1982);
C. Klopfenstein et al., Phys. Rev. Lett. **51**, 160 (1983);
S. Behrends et al., Phys. Rev. Lett. **52**, 799 (1984);
R. Nernst et al., Phys. Rev. Lett. **54**, 2195 (1985).
21) E. Eichten and F. Feinberg, Phys. Rev. **D23**, 2724 (1981);
W. Buchmuller, Phys. Lett. **112B**, 479 (1982).
22) C. E. Carlson and R. Suaya, Phys. Rev. **D18**, 760 (1978).
23) D. M. Kaplan, Ph. D. Thesis, State University of New York at Stony Brook, 1979.
24) D. G. Cassel, Cornel preprint CLNS-85/649 March (1985).
25) Addentum to Proposal 605, L.M.Lederman et al. (Nov. 1978)
26) Y. Sakai, Ph. D. Thesis, Kyoto University (1984);
Y. Sakai, Memoirs of the Faculty of Science, Kyoto University, Series of Physics, Astrophysics, Geophysics and Chemistry, Vol. **XXXVI**, No. 3, Article 2, p. 402, 1985.
27) H. Glass et al., IEEE Trans. Nucl. Sci. **NS-30, 30** (1983),
M. Adams et al., Nucl. Instr. & Method **217**, 237 (1983).
28) LN100 Nitrogen Laser Operating Manual, Photochemical Research Associates Inc., 45 Meg Drive, London, Ontario, Canada, N6E 2V2.
29) Hamamatsu TV Co., Ltd., 1126 Ichino-cho, Hamamatsu, Japan.
30) H. D. Glass, Ph. D.Thesis, State University of New York at Stony Brook, 1985.
31) J. A. Crittenden, Ph. D. Thesis, Columbia University, 1986;
Y. B. Hsiung, Ph. D. Thesis, Columbia University, 1986.
32) R. E. Plaag, Ph. D. Thesis, University of Washington, 1986.
33) J. A. Crittenden, JACTRACK(E605 Internal Report, March 1983).
34) Particle Data Group, Review of Particle Properties, **LBL-100** Revised, UC-34d, Apr. 1982.
35) A. L. S. Angelis et al., Nucl. Phys. **B209**, 284 (1982).
36) R. Brun et al., CERN DD/US/86, Revised June 1982.
CERN DD/US/85, July 1983.
37) A. Soni, Phys. Rev. **D8**, 2264 (1973);

J. Rutherfoord, Radiative Correction to the Dilepton Spectrum (E605 Internal Report, August 1986).
38) R. L. Ford and W. R. Nelson, SLAC-210, UC-32, June 1978.
39) J. D. Jackson, Classical Electrodynamics, John Wiley & Sons, Inc. 1962.;
Y. Sakai, private communication.
40) Particle Data Group, Particle Properties Data Booklet, April 1984;
A. S. Artamonor et al., Phys. Lett. **118B**, 225 (1981);
W. W. MacKay et al., Phys. Rev. **D29**, 2483 (1984);
D. P. Barber et al., Phys. Lett. **135B**, 498 (1984);
S. E. Baru et al., Z. Phys. **C30**, 551 (1986).
41) D. Andrews et al., Phys. Rev. Lett. **50**, 807 (1983).
42) J. G. H. de Groot et al., Z.Phys. **C1**, 143 (1979).
43) J. L. Rosner, Proceedings of the 1985 International Symposium on Lepton and Photon Interactions at High Energies, p.448, Kyoto, 1985.
44) W. J. Stirling, Proceedings of the Drell-Yan Workshop, p.131, Fermilab, 1982.
45) V. Barger and W. Y. Keung, Z.Phys. **C6**, 169 (1980);
V. Barger and W. Y. Keung, Phys. Lett. **91B**, 253 (1980).
46) Particle Data Group, Particle Properties Data Booklet, April 1986.
47) R. Baier and R. Ruckl, Z. Phys. **C19**, 251 (1983).
48) G. Altarelli et al., Phys. Lett. **151B**, 457 (1985).
49) L. Camilleri, Proceedings of the 1979 International Symposium on Lepton and Photon Interaction at High Energies, 1979, p.232.
50) C. Kourkoumelis et al., Phys. Lett. **91B**, 481 (1980).
51) J. Badier et al., Phys. Lett. **86B**, 98 (1979).
52) S. Childress and J. P. Rutherfoord, Phys. Rev. Lett. **54**, 2273 (1985).